Journal of Molecular Recognition

WILEY

Journal of Molecular Recognition

RESEARCH ARTICLE OPEN ACCESS

Nanohydrogel of Curcumin/Berberine Co-Crystals Induces Apoptosis via Dual Covalent/Noncovalent Inhibition of Caspases in Endometrial Cancer Cell Lines: The Synergy Between Pharmacokinetics and Pharmacodynamics

Feiyan Yan[1] | Yan Wang[1] | Lin Chen[1] | Wei Cheng[1] | Ernest Oduro-Kwateng[2] | Mahmoud E. S. Soliman[2] | Ting Yang[1]

[1]Department of Gynecology, The Second Affiliated Hospital of Xi'an Medical University, Xi'an, China | [2]Molecular Bio-Computation and Drug Design Research Group, School of Health Sciences, University of KwaZulu Natal, Westville Campus, Durban, South Africa

Correspondence: Ting Yang (yangtdoctor@outlook.com)

Received: 27 December 2024 | **Revised:** 1 February 2025 | **Accepted:** 3 March 2025

Funding: The authors received no specific funding for this work.

Keywords: covalent inhibition | dual binding | endometrial cancer | in silico | in vitro | molecular docking | molecular dynamics | natural products

ABSTRACT

Endometrial cancer remains a significant therapeutic challenge due to drug resistance and heterogeneity. This study leverages the synergistic potential of curcumin (CUR) and berberine (BBR) co-crystals encapsulated in a nanohydrogel to address these challenges through a pharmacokinetically and pharmacodynamically targeted therapeutic strategy. The nanohydrogel formulation significantly improves the solubility, stability, and bioavailability of CUR/BBR co-crystals, optimizing their therapeutic delivery and sustained release under physiological and tumor microenvironment conditions. On the other hand, the dual inhibitory mechanism of CUR and BBR, with CUR covalently binding to the active site of caspase-3 and BBR non-covalently targeting the allosteric site, achieves enhanced apoptotic activity by disrupting both the catalytic and conformational functions of caspase-3. In vitro cytotoxicity assays demonstrate remarkable efficacy of the CUR/BBR nanohydrogel, achieving an IC50 of 12.36 μg/mL against HEC-59 endometrial cancer cells, significantly outperforming the individual components and the standard drug Camptothecin (IC50: 17.27 μg/mL). Caspase-3/7 assays confirm enhanced apoptosis induction for the nanohydrogel formulation compared to co-crystals alone and Camptothecin. Molecular dynamics simulations and binding free energy analyses further validate the synergistic interaction of CUR and BBR in their dual binding mode. This study introduces a novel therapeutic approach by enhancing drug delivery and dual targeting mechanisms, demonstrating the potential of CUR-BBR nanohydrogel as a robust therapy for EC. This strategy offers a promising platform for addressing drug resistance and improving outcomes in endometrial cancer therapy.

1 | Introduction

Endometrial cancer (EC) ranks as the sixth most prevalent cancer among women globally, and its incidence has increased by 132% over the past three decades. This increase is attributed to several factors, including an aging population, as well as increasing rates of obesity and diabetes, which are significant risk factors for the disease. In 2020 alone, more than 417,000 new cases were reported [1, 2]. A defining characteristic of EC is its heterogeneity, which complicates its prognosis and treatment strategies. The advent of targeted therapies offers more precise and effective treatments than traditional methods, such as chemotherapy, immunotherapy, and radiation therapy. Notable examples include inhibitors of the PI3K/AKT/mTOR pathway

(example; everolimus), HER2 inhibitors, such as trastuzumab for HER2-positive tumors, and hormonal therapies targeting estrogen receptors [3]. Additionally, DNA damage response inhibitors, such as PARP inhibitors and immune checkpoint inhibitors, such as pembrolizumab, show promise in treating mismatch repair-deficient cancers. However, these therapies are not without limitations, such as tumor heterogeneity and the development of drug resistance [4]. Therefore, exploring additional molecular targets and pathways, such as those involved in the tumor microenvironment, metabolic vulnerabilities, and apoptotic regulation, remains critical.

Caspase-3, a critical effector in the apoptotic pathway, plays a significant role in the progression and aggressiveness of endometrial cancer (EC) [5, 6]. It was demonstrated that caspase-3 expression increases progressively from benign conditions to malignant carcinoma stages, with elevated levels correlating with poorer patient survival, particularly in tumors exhibiting over 50% caspase-3 positivity. The association of caspase-3 with the CAS gene and Bax highlights its involvement in a complex apoptotic regulatory network contributing to EC's aggressiveness [7]. A study by Wang et al. revealed that treatment with TWEAK activated caspase-3 and caspase-7, as well as caspase-8 and caspase-9, indicating its role in apoptosis via both extrinsic and intrinsic pathways [8]. Recent findings showed that KIF23 knockdown enhances apoptosis in EC by upregulating caspase-3, emphasizing its importance in overcoming apoptotic resistance. These studies underscore the pivotal role of caspase-3 in EC progression and its potential as a therapeutic target [9].

Most interestingly, caspases are a unique family of cysteine proteases that possess distinct active sites for catalysis and allosteric sites that regulate their functions, offering opportunities for dual-targeted therapeutic approaches [10, 11].

Multiple target therapy in cancer treatment represents a strategic evolution in cancer therapy at a molecular level [12]. This approach can be broken down into two primary methodologies: targeting one single protein or targeting multiple different proteins.

Targeting multiple different proteins involves a strategy where drugs or therapeutic agents are designed to interact with several distinct molecular targets [13, 14]. This method acknowledges the complexity of cancer biology, where tumors often rely on multiple signaling pathways for growth, survival, and metastasis.

On the other hand, targeting one single protein does not necessarily mean the therapy is singular in its approach. Instead, it often refers to therapies that focus on a single molecular target but use different mechanisms or drugs to modulate that target in multiple sites or mechanisms. For example, multiple drugs can target a protein through different mechanisms: one might inhibit its phosphorylation, another might block its dimerization, and yet another might promote its degradation.

Targeting a single protein at two distinct sites—such as an active site and an allosteric site—offers a powerful and strategic approach in drug discovery to enhance therapeutic efficacy and overcome resistance. By simultaneously engaging multiple sites on the same protein, this dual-binding strategy can disrupt critical functions more effectively than single-site targeting [15–17]. For instance, covalent binding at the active site ensures strong and often irreversible inhibition of enzymatic activity, while non-covalent binding at an allosteric site can induce conformational changes that further impair protein function or enhance inhibitor specificity. This dual-site targeting not only amplifies the inhibitory effect but also reduces the likelihood of resistance development, as it necessitates multiple simultaneous mutations in the protein to escape inhibition. In drug discovery, this approach has significant applications in tackling resistance mechanisms in diseases like cancer and infectious diseases, where adaptive changes in the target protein often undermine single-agent therapies [16–18]. By leveraging dual-site targeting, researchers can design more robust and effective therapeutics that capitalize on synergistic interactions, ultimately improving treatment outcomes and addressing the challenges posed by drug resistance. Several success stories of this approach exist. For example, a recent study showed that compound LP-168 serves as an innovative next-generation inhibitor of Bruton Tyrosine Kinase (BTK) that employs both covalent and non-covalent binding mechanisms. This dual-action inhibitor demonstrates promising results in patients with relapsed or refractory B-cell Non-Hodgkin Lymphoma [19, 20]. Another study focused on exploring the potential of dual binding of SMTIN-C10 to both orthosteric and allosteric sites to enhance the anticancer activity of a drug targeting Tumor Necrosis Factor Receptor-Associated Protein 1 (TRAP1). The dual binding mechanism of SMTIN-C10 significantly increased the potency of the drug against cancer cells. This was attributed to the synergistic effect of blocking ATP binding and the allosteric site [21]. Our previous research has explored the advantages of dual targeting and its impact on binding affinity and protein dynamics, highlighting the strategic value of this approach in drug design, especially for complex diseases like cancer [17, 18, 22].

In this study, we propose curcumin (CUR) and berberine (BBR), two bioactive compounds derived from natural products, as an optimal combination for achieving dual covalent and non-covalent interactions with established anticancer efficacy against endometrial cancer (EC). The study design is depicted in Figure 1. This selection is supported by the distinct and complementary mechanisms of action exhibited by these compounds. Curcumin, a polyphenol extracted from *Curcuma longa*, demonstrates the unique capability to form covalent bonds with active-site cysteine residues, thereby directly targeting enzymatic activity. In contrast, berberine, an alkaloid obtained from *Berberis species*, exerts its effects through non-covalent binding to allosteric sites, modulating protein conformation and function. Both curcumin [23] and berberine [24] have been extensively studied for their anticancer properties, including the ability to inhibit cancer cell proliferation and induce apoptosis across various cancer types, including EC. The chemopreventive potential of the co-treatment of CUR and BBR against breast cancers showed that CUR and BBR in combination synergistically inhibited the growth of both MCF-7 and MDA-MB-231 breast cancer cells more than the compounds used alone [25]. The combination of curcumin and berberine has also proven to be more effective in inhibiting the growth and proliferation of

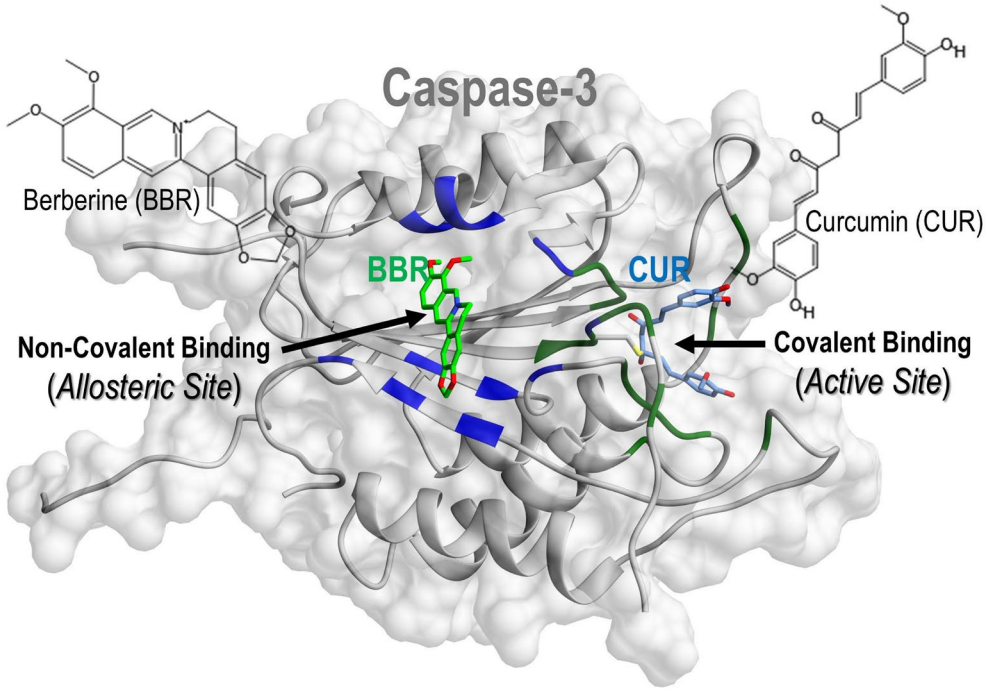

FIGURE 1 | The study design sketch showing the dual targeting of caspase by CUR and BBR in the active site and allosteric site, covalently and non-covalently, respectively. The 3D structure is created based on the results of this work.

cancer in the liver, breast, lung, bone, blood, and glioblastoma [26]. Despite previous research endeavors, this study, to the best of our knowledge, is the first to specifically leverage the structural characteristics of curcumin and berberine. We explore the covalent bonding capabilities of curcumin alongside the non-covalent interactions of berberine, integrating these features in a novel manner.

These complementary mechanisms highlight the therapeutic potential of this combination for targeting EC through synergistic dual-binding interactions.

Despite the remarkable anticancer activity of curcumin and berberine across various cancer types, their clinical application is hindered by challenges such as poor solubility and limited bioavailability [27, 28]. To address these limitations, we propose an innovative dual-binding strategy that leverages the complementary properties of curcumin and berberine (CUR-BRR) co-crystals, encapsulated within a nanohydrogel formulation. This approach combines the advantages of crystallization with advanced drug delivery systems to enhance the physicochemical properties of these bioactive compounds. Co-crystallization is a well-established technique that improves solubility, stability, and bioavailability, while also enabling controlled release profiles. Encapsulation within a nanohydrogel further enhances these benefits by providing a protective matrix that ensures targeted delivery, prolonged circulation time, and reduced degradation in biological environments [29]. Clinical scalability of nanohydrogel systems involves several key considerations for moving from research to clinical application, with advances in polymerization and automation allowing for consistent quality production, as discussed by Yu et al. (2016) for biomimetic hydrogels [30].

Together, this dual-covalent/non-covalent binding strategy represents a promising therapeutic innovation for maximizing the anticancer potential of CUR-BER against challenging diseases such as endometrial cancer.

In this study, we report the synthesis, formulation, and characterization of a nanohydrogel encapsulating curcumin/berberine (CUR/BBR) co-crystals, along with an evaluation of its in vitro anticancer activity against the endometrial cancer cell lines HEC-59 and its impact on caspase activity. Furthermore, molecular docking, molecular dynamics simulations, and thermodynamic binding affinity analyses were performed to elucidate the dual binding mechanisms underlying its therapeutic efficacy. This comprehensive investigation would provide a comprehensive understanding of the nanohydrogel potential of CUR/BBR co-crystals as a novel therapeutic strategy for endometrial cancer.

2 | Materials and Methods

The workflow of this study is depicted in Figure 2.

2.1 | Experimental Methodology

2.1.1 | Materials and Reagents

Curcumin (CAS: 458-37-7) and berberine chloride hydrate (CAS: 633-65-8), both with HPLC purity >95%, were sourced from Toronto Research Chemicals Inc. (Toronto, ON Canada) and stored under manufacturer specifications for use. The purity and specifications of the other materials were verified prior to use.

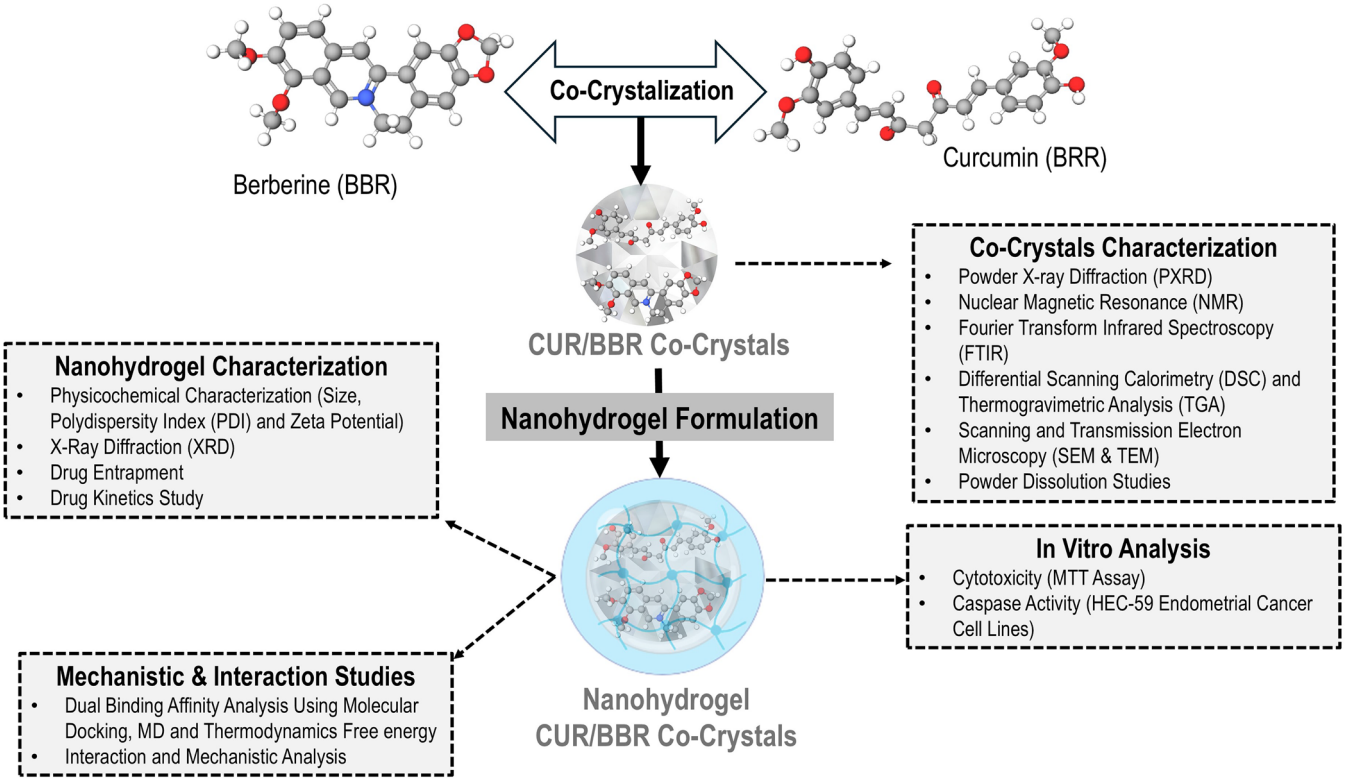

FIGURE 2 | The workflow of the different techniques and methods adopted in the current study. Some of the image components were adopted from [31].

2.1.2 | Preparation of Curcumin-Berberine (CUR-BBR) Co-Crystals

Curcumin-berberine (CUR-BBR) co-crystals were prepared using the liquid-assisted grinding (LAG) method according to previous studies [32, 33]. A 1:1 M ratio of curcumin and berberine was weighed and manually ground in an agate mortar. Methanol was added dropwise to aid the grinding process. The mixture was ground for 20 to 60 min, with intermittent pauses every 15 min for 2 min to prevent overheating. After grinding, the mixture was transferred to a vacuum oven (IncoTherm, Labotec) and dried at 40°C for 24 h to remove residual solvent. The resulting co-crystals were collected and stored for further characterization.

2.1.3 | Characterization of Curcumin-Berberine (CUR-BBR) Co-Crystals

2.1.3.1 | Powder X-Ray Diffraction (PXRD). PXRD analysis was performed to confirm the formation of a unique crystalline phase for CUR-BBR co-crystals. XRD patterns were recorded on a MiniFlex600-PXRD (Rigaku Analytical Devices, USA) operating at 40 kV and 15 mA. Data were collected over a 2θ range of 5° to 90° at a scan speed of 0.01°2θ s^{-1}, using Cu Kα radiation ($\lambda = 1.54$ Å) with a secondary graphite monochromator. Patterns were analyzed with SmartLab Studio II.

2.1.3.2 | Nuclear Magnetic Resonance (NMR) Spectroscopy. The samples were dissolved in DMSO-d_6 and run for ^{1}H NMR and ^{13}C NMR experiments. Nuclear magnetic resonance (NMR) spectra were recorded on a Bruker 600 MHz UltraShield spectrometer equipped with a 5 mm TXI probe. All spectra are reported with the chemical shifts in parts per million (ppm) and the samples were dissolved in DMSO-d_6. hence, the DMSO-solvent peak is shown in all spectra. The multiplicity is observed in proton spectra and reported as singlet (s), doublet (d), triplet (t) and broad peaks (br).

2.1.3.3 | Fourier Transform Infrared Spectroscopy (FTIR). FTIR spectra were analyzed to identify molecular interactions between curcumin and berberine in the co-crystals. Samples were scanned from 4000 to 400 cm^{-1} via the pressed-disc procedure using (Bruker Alpha-PATR–FT-IR, Germany).

2.1.3.4 | Differential Scanning Calorimetry (DSC) and Thermogravimetric Analysis (TGA). The thermal behavior of the CUR-BBR co-crystals and individual components was analyzed using Differential Scanning Calorimetry (DSC) and Thermogravimetric Analysis (TGA) on a Shimadzu DSC-60 (Japan). Approximately 2 mg of each sample was placed in an aluminum pan and sealed with a crimper. The samples were heated from ambient temperature to 300°C at a constant rate of 10°C/min under a nitrogen flow of 20 mL/min. An empty aluminum pan was used as a reference [34].

2.1.3.5 | Scanning and Transmission Electron Microscopy (SEM & TEM). Morphological characterization was performed using FEG-SEM (ZEISS Ultra Plus, Germany) at 10 kV and high-resolution transmission electron microscopy (HR TEM) (JEOL 2100, USA) operating at 100 kV.

Energy-dispersive X-ray spectroscopy (EDX) was employed for elemental composition analysis using a ZEISS Ultra Plus FEG SEM (Germany) integrated with Oxford INCA and Aztec EDX Analysis Software.

2.1.3.6 | Powder Dissolution Studies. Dissolution studies were conducted to compare the solubility of CUR-BBR cocrystals with pure curcumin and berberine using the shaking flask method [35]. A standard mass (30 mg) of each sample was added to separate vials containing 5 mL of phosphate-buffered saline (PBS) at pH 7.4 and 4.5. The vials were placed in an orbital shaker at 37°C ± 0.5°C for 48 h. After incubation, the solutions were filtered through a 0.22 μm syringe filter to remove any undissolved particles. The concentration of the dissolved samples was quantified using UV–Vis spectrophotometry at λ_{max} 424/266 nm (Shimadzu UV-1800, USA). The solubility studies were conducted in triplicate.

2.1.4 | Preparation of Curcumin-Berberine (CUR-BBR) Co-Crystal–Loaded Chitosan Nanohydrogel (CUR-BBR/CSNH)

Curcumin-berberine (CUR-BBR) co-crystal-loaded chitosan nanohydrogels (CUR-BBR/CSNH) were synthesized using a modified ionic gelation technique [36]. A chitosan solution was prepared by dissolving chitosan (0.3125% w/v) in 1% (v/v) acetic acid. The solution was stirred for 12 h at pH 4.7 to facilitate gelation. Simultaneously, a 0.2% (w/v) aqueous solution of tripolyphosphate (TPP) was prepared and added dropwise to the chitosan solution while stirring for 30 min, initiating the ionic gelation process and resulting in the formation of the chitosan-based nanohydrogel (CSNH). To prepare the CUR-BBR/CSNH formulation, CUR-BBR co-crystals were dissolved in methanol and incorporated into the chitosan solution dropwise prior to the addition of TPP. The mixture was stirred continuously for 12 h to ensure efficient encapsulation of the CUR-BBR co-crystals within the CSNH matrix. Both CUR-BBR/CSNH and CSNH formulations were subsequently subjected to sonication at 30 kHz for 10 min to improve particle homogeneity and dispersion. The resulting CUR-BBR/CSNH and CSNH formulations were stored at 4°C for further analysis and use. The synthesis conditions, including chitosan and TPP concentrations, as well as CUR-BBR co-crystal content, were optimized to achieve the desired properties in terms of hydrogel formation, stability, and drug release profiles.

2.1.5 | Characterization of Curcumin-Berberine (CUR-BBR) Co-Crystal–Loaded Chitosan Nanohydrogel (CUR-BBR/CSNH)

The Curcumin-berberine (CUR-BBR) co-crystal-loaded chitosan nanohydrogel (CUR-BBR/CSNH) formulation was assessed using various analytical techniques, including X-ray diffraction (XRD); the size, polydispersity index (PDI), and zeta (ζ) potential were evaluated to assess the particle characteristics, while encapsulation efficiency was determined to gauge the effectiveness of the formulation. Additionally, in vitro drug release studies were conducted to analyze the release profile of CUR-BBR from the nanohydrogel system [37].

2.1.5.1 | Size, Polydispersity Index (PDI), and Zeta (ζ) Potential. The size, polydispersity index (PDI), and zeta (ζ) potential of the prepared Curcumin-berberine (CUR-BBR) co-crystal-loaded chitosan nanohydrogel (CUR-BBR/CSNH) were determined using dynamic light scattering (DLS) and zeta potential analysis with a Malvern Zetasizer Nano range apparatus (Malvern Instruments Ltd., Malvern, U.K.). A 1 mL sample of the formulation was analyzed in polystyrene cuvettes (DTS0012, Malvern Instruments) at 25°C, with a scattering angle of 90°. All measurements were performed in triplicate.

2.1.5.2 | Entrapment Efficiency. The entrapment efficiency of the Curcumin-berberine (CUR-BBR) co-crystal-loaded chitosan nanohydrogel (CUR-BBR/CSNH) formulation was determined as follows [38]. A 3 mL volume of the CUR-BBR/CSNH formulation was transferred to an Amicon Ultra Centrifugal Filter (10 kDa MWCO; UFC8010; Merck Millipore Ltd., Cork, Ireland) and subjected to centrifugation at 3000 rpm, 25°C, for 10 min to separate the free drug. The concentration of the free drug in the filtrate was quantified using UV–Vis spectrophotometry at 424/266 nm (Shimadzu UV-1800, USA). The entrapment efficiency (%EE) was calculated using the equation:

$$\text{Entrapment efficiency}\,(\%\,\text{EE}) = \left(\frac{\text{Total Drug} - \text{Free Drug}}{\text{Total Drug}}\right) \times 100$$

2.1.5.3 | Drug Kinetic Study. The drug release profile of Curcumin-berberine (CUR-BBR) co-crystal-loaded chitosan nanohydrogel (CUR-BBR/CSNH) was investigated using the dialysis method [39]. Dialysis tubing (cellulose membrane, 14 kDa MWCO; UFC8010; Sigma-Aldrich) was soaked in double-distilled water for 12 h prior to use. Dialysis bags containing 2 mL of the test sample were clamped at both ends and immersed in 40 mL of phosphate-buffered saline (PBS) at pH 7.4 and 4.5, placed in Falcon conical tubes (Corning, New York, USA), and kept in an orbital shaker at 37°C ± 0.5°C for 48 h. Aliquots of 3 mL were withdrawn from the release medium at intermittent time intervals (30 min, 1, 2, 3, 4, 5, 6, 7, 8, 12, 24, and 48 h) and replaced with an equal volume of fresh dissolution media to maintain a constant volume. The water bath was maintained at the set temperature. The concentration of released CUR-BBR co-crystals was quantified using UV–Vis spectrophotometry at 424/266 nm (Shimadzu UV-1800, USA). All measurements were conducted in triplicate. The cumulative release of CUR-BBR from CUR-BBR/CSNH was calculated using the following formula:

$$\text{Cumulative Release}(\%) = \frac{\sum_{t=0}^{t} M_t}{M_0} \times 100$$

Where M_t represents the amount of CUR-BBR released at time t, and M_0 is the initial amount of the drug.

2.1.5.4 | X-Ray Diffraction (XRD). For the X-ray diffraction (XRD) analysis of the nanohydrogel, the sample was freeze-dried to obtain a powdered form, which was then finely ground to ensure uniformity. The powder was spread evenly on a glass substrate for analysis. The XRD instrument was configured with Ni-filtered Cu Kα radiation, operating at a voltage

of 40 kV and a current of 20 mA. Measurements were performed over a 2θ range of 2°–50° with a step size of 0.02° and a scan rate of 4°/min. The sample was placed on the instrument stage, and diffraction patterns were recorded. The collected data was analyzed to identify characteristic peaks and assess the crystalline structure, with results compared to reference patterns for interpretation [36].

2.2 | In Vitro Studies

2.2.1 | Cell Culture

Endometrial cancer cell lines (HEC-59) were cultured in Iscove's Modified Dulbecco's Medium (IMEM) containing 2 mM L-glutamine and 25 mM HEPES (Gibco) at 37°C in a 5% CO_2 humidified incubator. Human Embryonic Kidney (HEK293) cells were cultured in Dulbecco's Modified Eagle Medium (DMEM) containing 4.5 g/L D-glucose, L-glutamine, and pyruvate (Gibco). Both media were supplemented with 10% heat-inactivated and gamma-irradiated Fetal Bovine Serum (FBS) (Gibco) and 1% Penicillin–Streptomycin (Gibco). Once cells reached approximately 80% confluency, they were washed with Phosphate Buffered Saline (PBS) pH 7.4, containing calcium chloride and magnesium chloride (Gibco), trypsinized with 0.25% Trypsin–EDTA (Gibco), and subcultured [40].

2.2.2 | Cell Viability Assay

Cell viability was assessed using the 3-(4,5-dimethylthiazol-2-yl)-2,5-diphenyltetrazolium bromide (MTT) assay to evaluate the cytotoxic effects of CUR-BBR co-crystals on both HEC-59 and HEK293 cell lines, as described in previous studies [41, 42]. 100 μL of cell culture (1×10^5 cells/mL) was seeded into each well of a 96-well microtiter plate. The cells were allowed to incubate for 24 h at 37°C in a humidified 5% CO_2 environment. Following incubation, the culture medium was removed, and 10 μL of each test compound was added to the wells in serial concentrations ranging from 1 to 0.0078125 mg/mL. Stock solutions of CUR-BBR co-crystals were prepared in DMSO, and serial dilutions were made with fresh culture medium. A 0.1% DMSO solution was used as the negative control, while camptothecin was used as a positive control at the same serial concentrations. Treatments were performed in triplicates. The plates were incubated for an additional 48 h under the same conditions.

After incubation, 10 μL of MTT solution (5 mg per 1 mL of DMSO) was added to each well, and the plates were incubated for 4 h at 37°C in a 5% CO_2 atmosphere. Following the incubation, the MTT solution was removed, and 100 μL of DMSO was added to each well to solubilize the formazan crystals formed by viable cells. The plates were incubated for 1 h to ensure complete dissolution. The absorbance of each well was then measured at 570 nm using a microplate spectrophotometer (Multiscan Go, Thermo Scientific).

The percentage cell viability, cytotoxicity, and drug inhibition were determined using the following formulas:

$$\%\text{Cell Viability} = (\text{Absorbance of treated cells}) / (\text{Absorbance of untreated cells}) \times 100$$

$$\%\text{Drug Inhibition} = ((\text{Absorbance of untreated cells}) - (\text{Absorbance of treated cells})) / (\text{Absorbance of untreated cells}) \times 100$$

The percentage of cell viability and inhibition was calculated for each treatment, and the IC_{50} values were determined through nonlinear regression analysis. MTT assays were performed for curcumin and berberine individually, and all experiments were conducted in triplicate.

2.2.3 | Caspase 3/7 Glo Assay

Caspase-3/7 activity was assessed using the Caspase-Glo 3/7 Assay (Promega), following the manufacturer's protocol [41]. The assay utilizes a luminogenic caspase-3/7 substrate in a buffer solution to quantify caspase activity in cell lysates. The level of caspase activity is directly correlated with the luciferase signal generated. HEC-59 cells were seeded at a density of 20,000 cells/well in a white 96-well plate and incubated overnight at 37°C with 5% CO_2 in DMEM with 10% FBS. Following incubation, the cells were treated with the IC50 concentration of the CUR/BBR co-crystals, nanohydrogel formulation, and Camptothecin. Subsequently, Caspase-GloTM-3/7 reagents were added to the cells in the 96-well plates and incubated for 60 min. Luminescence was measured using a plate reader. All experiments were performed in triplicate, and the results are presented as relative light units (RLU).

2.3 | Computational Methodology

2.3.1 | CUR/BBR Co-Crystal Modelling

The 3D coordinates of CUR and BBR were obtained from PubChem (CID: 969516 and CID: 2353, respectively) then imported into Avogadro software (https://avogadro.cc/). A conformational search tool in Avogadro was used to search for the most favorable spatial orientation of CUR and BBR. This was followed by energy optimization at the B3LYP/6-31G(d,p) level of theory using Gaussian 09 (https://gaussian.com/). The resulting optimized structures are showcased in the Supporting Information (Figure S6A,B).

2.3.2 | Preparation of Protein and Ligands

The three-dimensional (3D) crystallized structure of human caspase-3 in complex with a sulfonamide inhibitor (MSI) at the catalytic site (PDB: 1GFW) resolved via X-ray diffraction at 2.80 Å resolution was retrieved from RCSB Protein Data Bank. In the absence of a crystal structure of caspase-3 in complex with a ligand at the allosteric binding site, the binding coordinates of human caspase-7 resolved at 2.80 Å (PDB: 1SHJ) was used as a template, due to its high structural similarity and biological function to caspase-3 [11, 43]. The caspase-7 structure in complex with DICA, a covalent ligand bound in a

cis-orientation, was selected, as DICA shows greater potency against both caspase-3 and caspase-7 compared to FICA, which binds in a trans-orientation [10]. The protein preparation wizard in UCSF Chimera 1.18 was used, which included the removal of water and nonstandard molecules. Hydrogen atoms were added, and the system was neutralized to ensure proper charge distribution [44]. The protonation state of the protein at physiological pH was predicted using the H++ server (http://newbiophysics.cs.vt.edu/H++/) [45]. Structural corrections were made, including conversion of selenomethionine (MSE) to methionine (MET), bromo-UMP (5BU) to UMP (U), methylselenyl-dUMP (UMS) to UMP (U), and methylselenyl-dCMP (CSL) to CMP [46].

The 3D structures of curcumin (CID: 969516) and berberine (CID: 2353) were retrieved from PubChem in Structure-Data Format (SDF) files. Ligand preparation involved energy minimization using UCSF Chimera tools, applying 100 steepest descent steps (0.02 Å step size), followed by 10 conjugate gradient steps (0.02 Å step size), with Gasteiger charges calculated using the ANTECHAMBER tool.

2.3.3 | Molecular Docking Simulations

In the present study, we investigated the molecular mechanics of CUR-BER co-crystals with caspase-3 to explore their potential to induce apoptosis in an EC cell line (HEC-59). Caspase-3 was selected as the primary target because of its broad substrate specificity and central role in executing apoptotic signaling. Unlike caspases-6 and -7, which play supplementary or redundant roles in inflammation and stress responses, the unique role of caspase-3 makes it ideal for focused therapeutic interventions in cancer [10].

Site-directed docking calculations were performed to target the defined binding sites on caspase-3, enhancing the precision of docking and minimizing the risk of false-positive interactions. Non-covalent docking simulations were conducted using AutoDock Vina 1.1.2, with docking grids centered on the catalytic and allosteric binding pockets at coordinates (37.7, 34.4, 29.0) and (30.5, 29.1, 43.4) (X, Y, Z), respectively. The binding sites were identified based on the position of co-bound ligands in the crystal structure of caspase-3 (catalytic site: PDB 1GFW and allosteric binding site: PDB: 1SHJ). The grid box dimensions for the catalytic and allosteric sites were ($23.9 \times 19.4 \times 22.3$ Å) and ($23.6 \times 18.6 \times 18.3$ Å), respectively. The protein was kept rigid during the docking process, while the ligands were treated as fully flexible to explore various binding conformations [47].

Covalent docking simulations were performed using Maestro 13.6, part of the Schrödinger 2023-2 software suite, and Glide for high-precision docking calculations [48]. In these simulations, curcumin was covalently docked to the reactive C163 and C264 residues at the catalytic and allosteric sites, respectively, via a Michael addition reaction. The docking grids were defined with centers at coordinates (34.7, 32.9, 34.8) and (35.4, 28.4, 38.9) for the catalytic and allosteric pockets, respectively. The docking protocol was validated by redocking the co-crystallized ligand, showing complete structural alignment in the binding pockets (Figure S1A,B). Docking poses were evaluated based on their calculated binding free energy, with the most favorable interactions selected for further analysis.

2.3.4 | Molecular Dynamics Simulations

To explore the structural dynamics and thermodynamic perturbations of caspase-3 upon inhibition, we conducted molecular dynamics (MD) simulations using AMBER 18 with GPU acceleration (PMEMD.CUDA) [49]. The ligands were parameterized using the ANTECHAMBER protocol, with partial charges derived from the restrained electrostatic potential (RESP) method and the General Amber Force Field (GAFF). The caspase-3 structure was prepared using the pdb4amber command, followed by solvation in a TIP3P water box with 12 Å padding and neutralization using sodium and chloride ions to mimic physiological conditions. Two stages of energy minimization were performed: an initial 2500-step minimization with a 500 kcal/mol restraint to stabilize the system, followed by a 200-step unconstrained minimization. The system was then heated from 0 to 300 K over 50 ps in the NVT ensemble using a Langevin thermostat with harmonic restraints of 10 kcal/mol Å. Equilibration was achieved by applying a pressure of 1 bar with a Berendsen barostat and constraining hydrogen bonds via the SHAKE algorithm. Production simulations were conducted for 200 ns at 300 K and 1 bar in the NPT ensemble, using a 2-fs time step. Structural stability and fluctuations were analyzed by calculating root mean square deviation (RMSD) and root mean square fluctuation (RMSF) using the CPTRAJ and PTRAJ modules in AMBER 18 [50].

2.3.5 | Binding Free Energy Calculations

The binding free energy (BFE) of the protein-ligand complexes was computed using the molecular mechanics generalized-born surface area (MM/GBSA) approach [51]. This method integrates molecular mechanics calculations, which consider van der Waals interactions, electrostatics, and internal energies, with the generalized Born (GB) model for polar solvation and surface area (SA) terms for non-polar solvation energy.

The binding free energy (ΔG_{bind}) is computed as:

$$\Delta G_{bind} = G_{complex} - G_{receptor} - G_{ligand}$$

$$\Delta G_{bind} = E_{gas} + G_{sol} - T\Delta S$$

$$E_{gas} = E_{int} + E_{vdw} + E_{ele}$$

$$G_{sol} = G_{GB} + G_{SA}$$

$$G_{SA} = \gamma \mathrm{SASA}$$

$G_{complex}$ is the free energy of the protein-ligand complex. $G_{receptor}$ and G_{ligand} are the free energies of the receptor and ligand, respectively. E_{gas} is the gas-phase energy, comprising the internal energy (E_{int}), van der Waals energy (E_{vdw}), and electrostatic energy (E_{ele}). G_{sol} is the solvation energy, including contributions from both polar and non-polar solvation. G_{GB} is

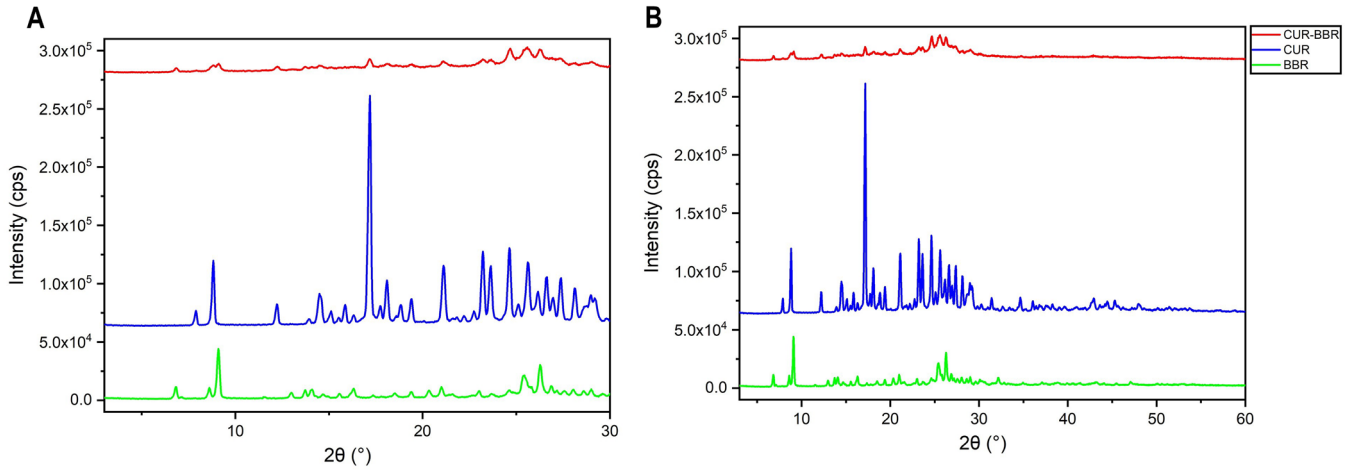

FIGURE 3 | X-ray diffraction (XRD) patterns of CUR-BBR co-crystals (red) overlaid with those of CUR (blue) and BBR (green) recorded over (A) 3°–30° and (B) 3°–60°2θ.

the polar solvation energy, calculated using the generalized Born (GB) model, which computes the solvation free energy based on the Born radii of atoms and their pairwise electrostatic interactions. G_{SA} is the non-polar solvation energy, determined by the solvent-accessible surface area (SASA) of the solute. G_{SA} is expressed by a surface tension constant (γ), 0.0072 kcal/mol·Å^2 and SASA is calculated using a 1.4 Å water probe radius. This term captures the hydrophobic interactions quantified through the buried surface area (BSA). TΔS is the entropy contribution, where ΔS is the system's entropy, estimated using normal mode analysis as implemented in AMBER Tools. The interaction entropy (−TΔS) was computed from 50,000 frames sampled during the simulation.

2.4 | Statistical Analysis

All statistical analyses, where applicable, were conducted using PrismPad, Microsoft Excel, and/or Statistical Product and Service Solutions (SPSS) version 20.0 software. One-way analysis of variance (ANOVA) was used for comparisons between multiple groups. The data are expressed as mean ± standard deviation (SD). A p-value of <0.05 was considered statistically significant.

3 | Results & Discussion

3.1 | Co-Crystallization and Characterization of CUR-BBR Co-Crystals

3.1.1 | PXRD Analysis

The PXRD patterns of CUR, BBR, and CUR-BBR co-crystals demonstrate differences suggestive of a new crystalline phase in the CUR-BBR co-crystals. The PXRD pattern of CUR exhibits sharp, intense peaks characteristic of a highly crystalline material. Major peaks observed from 10° to 30°, specifically at 8°, 17°, and 23°, reflect the well-defined crystalline structure of CUR [52]. BBR shows a different set of crystalline peaks (9°, 11°, 18° and 26°), although they are less intense and slightly broader compared to CUR, indicating a moderate degree of crystallinity [53]. The PXRD pattern of CUR-BBR co-crystals reveals a significant reduction in peak intensity and the near disappearance of sharp, distinct peaks observed for CUR and BBR individually (Figure 3A,B). The broader peaks and reduced intensities may suggest that CUR and BBR interact to produce a more amorphous or disordered structure in the co-crystal, suggestive of enhanced solubility and dissolution properties.

3.1.2 | NMR for Curcumin, Berberine and Co-Crystals

The samples were characterized by solution NMR to confirm their chemical structure (Supporting Information, Figures S2–S5). The samples were dissolved in DMSO-d_6 and run for ^{1}H NMR and ^{13}C NMR experiments. The preparation method and NMR experimental parameters were kept the same for both the co-crystals and individual compounds. The ^{1}H NMR spectrum of the co-crystal showed that most of the proton peaks have shifted upfield. This shift was also observed in the ^{13}C NMR spectrum. Some peaks did not shift, while some had a downfield shift (Figure 4A,B). The chemical shift that is observed in the proton and carbon NMR spectra for the co-crystal suggests that those protons and carbons are no longer in the chemical environment. This may be an indication that the compounds have co-crystalized.

3.1.3 | SEM and TEM Imaging

3.1.3.1 | SEM Analysis. The SEM image of CUR reveals crystalline structures with a well-defined, plate-like morphology (Figure 5A). The crystals are relatively uniform in size, with typical sharp edges and smooth surfaces. The SEM image of BBR shows a more irregular crystalline morphology compared to CUR. The particles appear as aggregated clusters with jagged edges and less uniformity, suggesting a lower degree of crystallinity or potential aggregation. In contrast to the individual components, the CUR –BBR co-crystals exhibit a unique morphology characterized by rough, fibrous structures and irregular aggregates (Figure 5A). This significant morphological

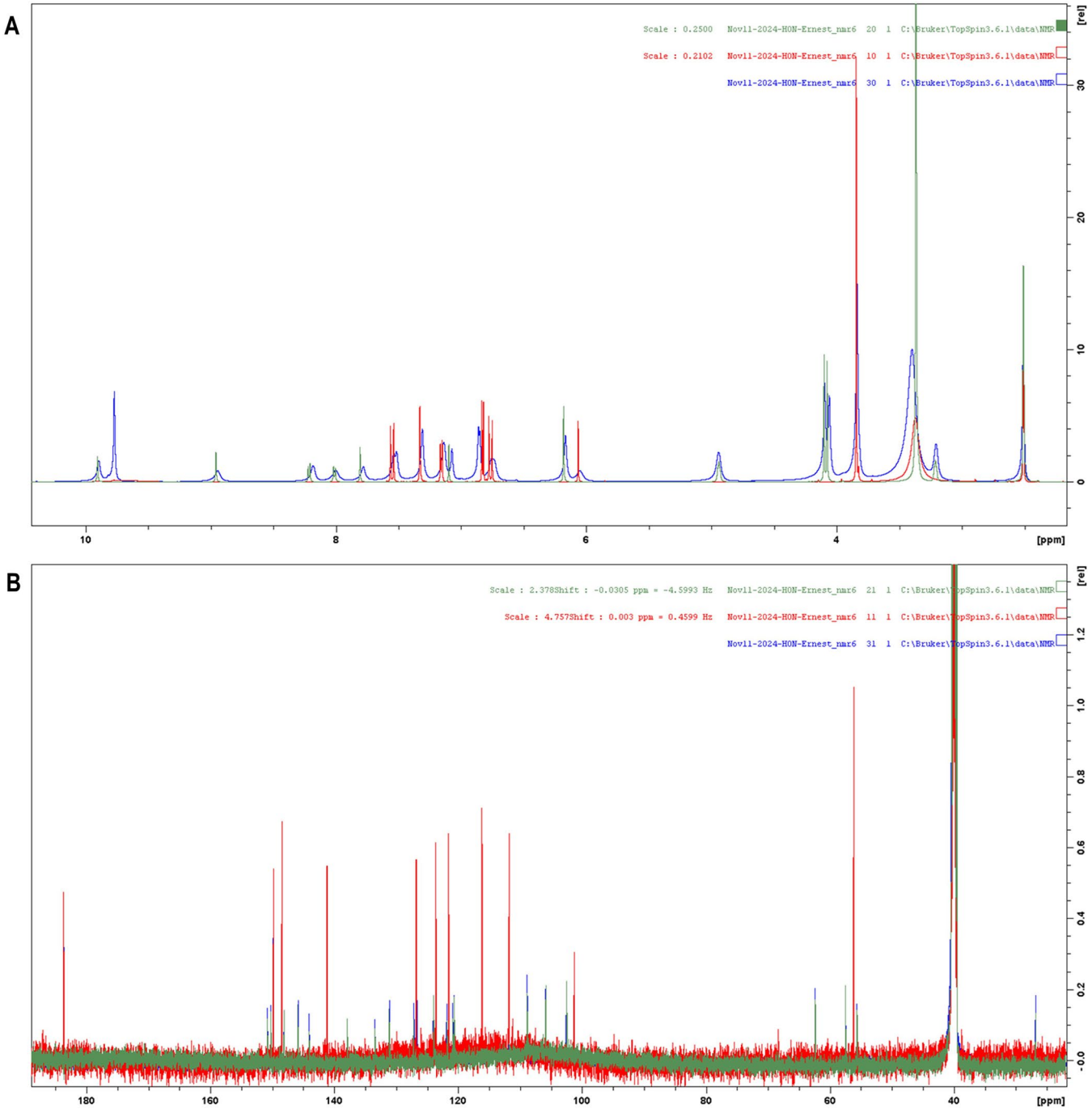

FIGURE 4 | (A) ^{1}H NMR and (B) spectrum of overlaid spectra of co-crystal (blue), curcumin (red) and berberine (green).

transformation confirms the formation of a new crystalline phase, distinct from the parent compounds.

3.1.3.2 | TEM Analysis. The TEM image of CUR shows densely packed particles with a relatively uniform size and smooth architecture. The particles maintain their crystalline integrity, as evidenced by their sharp boundaries. The TEM image of BBR displays amorphous or semi-crystalline aggregates with irregularly shaped particles. The lack of uniformity in size and texture aligns with the observations from SEM. The TEM image of CUR-BBR co-crystals demonstrates a significant change in morphology, with a less ordered, fused appearance (Figure 5B). The particles appear more amorphous, suggesting successful co-crystallization.

3.1.4 | FTIR, DSC and TGA

3.1.4.1 | FTIR Analysis. The FTIR spectra reveal significant shifts in characteristic vibrational frequencies, suggestive of intermolecular interactions in the CUR-BBR co-crystals. Key peaks for CUR include phenolic (—OH) stretching (3500 cm^{-1}), carbonyl (C═O) stretching (1623 to 1618 cm^{-1}), and aromatic C═C vibrations (1628 cm^{-1}), characteristic of its crystalline structure [54]. BBR displays absorption bands associated with alkaloid groups, such as methoxy (O—CH3) stretching (2844 cm^{-1}) and aromatic C═C bonds (1600 and 1475 cm^{-1}) [55]. The spectrum of the co-crystals exhibits notable shifts and changes in peak intensities, particularly in the C—H (2971 to 2944 cm^{-1})

and C═O (1698 to 1631 cm^{-1}) stretching regions. These shifts indicate the formation of hydrogen bonds or other intermolecular interactions between CUR and BBR molecules. The absence of major peaks corresponding to the pure components suggests the formation of a unique co-crystalline phase (Figure 6A).

3.1.4.2 | DSC Analysis. Thermal analysis through DSC further corroborates the distinct phase behavior of CUR-BBR co-crystals. The individual components exhibit endothermic peaks near 180°C–190°C and 200°C–210°C for CUR and BBR, respectively, corresponding to their melting points. The co-crystals display a new melting endotherm at 160°C–170°C, significantly lower than those of CUR and BBR (Figure 6B). This shift in thermal behavior indicates the successful formation of a co-crystal with unique thermal properties, potentially resulting in improved stability or altered solubility characteristics. Consequently, the lower melting point of the co-crystals may reflect improved packing efficiency and intermolecular interactions, consistent with the structural changes noted in FTIR and the fibrous morphology seen in SEM.

3.1.4.3 | TGA Analysis. The TGA profiles provide insights into the thermal stability and decomposition behavior of the test drugs. CUR exhibits a one-step degradation pattern, with decomposition starting around 300°C, while BBR begins to degrade at 250°C, showing slightly lower thermal stability. The co-crystals exhibit a single-step decomposition profile and demonstrate an intermediate thermal stability, with decomposition initiating at approximately 275°C (Figure 6C). This enhancement in stability compared to BBR can be attributed to improved molecular packing and interactions in the co-crystalline state. The absence of a multi-step process and the delayed degradation compared to BBR suggests improved stability due to co-crystallization.

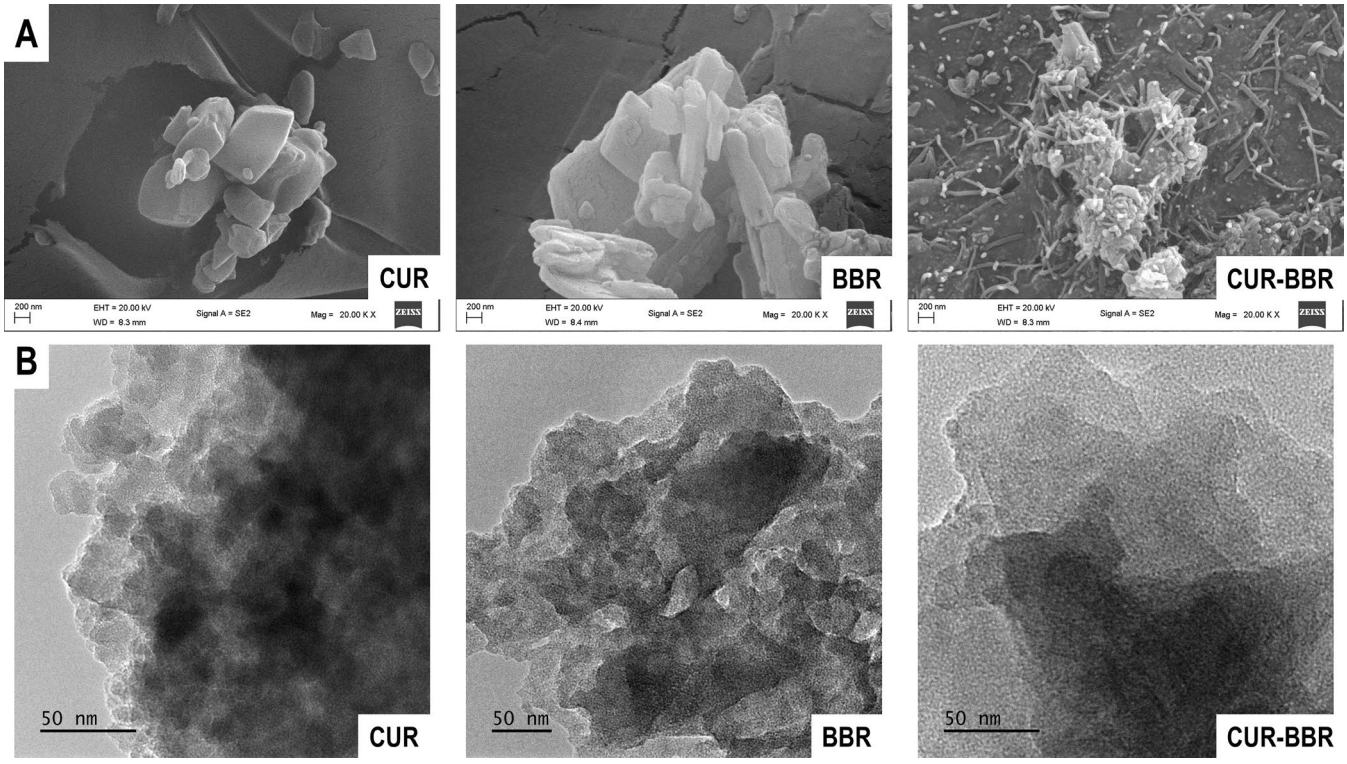

FIGURE 5 | Micrographs of (A) scanning electron microscopy (SEM) and (B) transmission electron microscopy (TEM) of CUR, BBR, and CUR-BBR co-crystals.

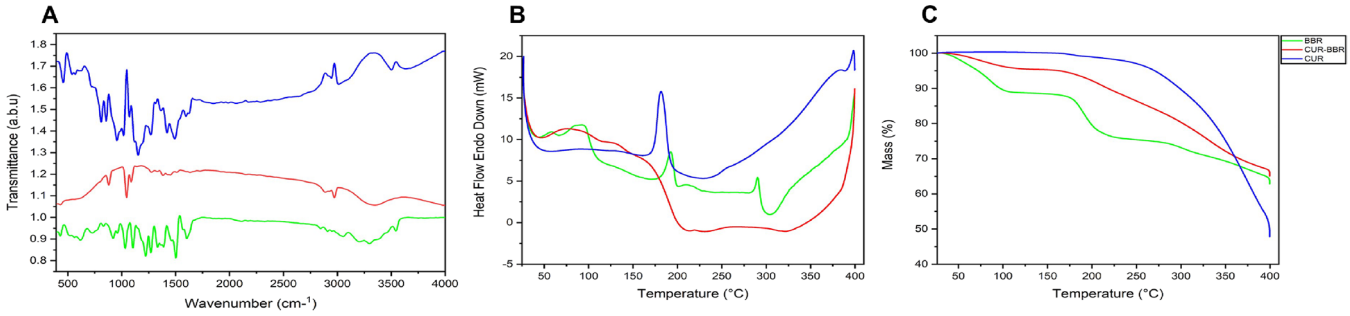

FIGURE 6 | Graph of (A) Fourier transform infrared spectroscopy (FTIR), (B) differential scanning colometry (DSC), (C) and thermogravimetric analysis (TGA) of CUR-BBR co-crystals (red) overlaid with those of CUR (blue) and BBR (green).

TABLE 1 | Mean solubility profiles of CUR, BBR, and CUR-BBR in PBS solution (pH 7.4 and pH 4.5) after 48 h of dissolution.

	Concentration (μg/ml)		
PBS environment	**CUR**	**BBR**	**CUR-BBR**
Ph 7.4	0.508	48.877	87.845
Ph 4.5	0.208	48.877	88.780

TABLE 2 | Physiochemical properties of CUR-BBR/CSNH and CSNH as indicative of a stable nanohydrogel system.

	CUR-BBR/CSNH	CSNH
Diameter (nm)	637.30	263.80
Polydispersity index (PDI)	0.188	0.60
Zeta potential (mV)	35.10	34.83

3.1.5 | Solubility Profiling of CUR-BBR Co-Crystals

The solubility profiling of curcumin (CUR), berberine (BBR), and the CUR-BBR co-crystal in phosphate-buffered saline (PBS) solutions at pH 7.4 and pH 4.5 demonstrates significant enhancement in the solubility of CUR in the co-crystal formulation (Table 1). CUR alone exhibited a remarkably low solubility of 0.508 μg/mL at pH 7.4 and 0.208 μg/mL at pH 4.5, reflecting its inherent poor aqueous solubility. In contrast, the CUR-BBR co-crystal achieved solubility levels of 87.845 μg/mL at pH 7.4 and 88.780 μg/mL at pH 4.5. This implies that the co-crystallization process effectively enhances CUR's solubility in both neutral and acidic environments. Interestingly, the solubility of BBR remained constant in both pH conditions (48.877 μg/mL), indicating that the improvement in the CUR-BBR co-crystal was predominantly due to CUR's altered dissolution behavior rather than changes in BBR's intrinsic solubility. Moreover, the size reduction observed in the co-crystals compared to the individual components is a critical factor in enhancing bioavailability, as smaller particle sizes facilitate improved solubility and dissolution rates. The findings have critical implications for improving the bioavailability of both CUR and BBR, as poor solubility is a key limiting factor for their therapeutic applications. Therefore, co-crystallization represents a promising strategy to overcome solubility limitations in both compounds [34, 53].

3.2 | Nanohydrogel Formulation and Characterization of CUR-BBR/CSNH

3.2.1 | Particle Size, Zeta Potential and Polydispersity Index (PDI)

The characterization of Curcumin-Berberine (CUR-BBR) Co-crystal–Loaded Chitosan Nanohydrogel (CUR-BBR/CSNH) revealed significant insights into the structural and functional properties of the formulation (Table 2). The particle size of CUR-BBR/CSNH was observed to be 637.3 nm, which was notably larger compared to the 263.8 nm size of unloaded chitosan nanohydrogel (CSNH). This increase in size can be attributed to the successful encapsulation of the CUR-BBR co-crystal within the chitosan nanohydrogel matrix [56]. The larger size of CUR-BBR/CSNH implies a potential increase in drug-loading capacity and stability, which may enhance the bioavailability and retention time of CUR-BBR. The polydispersity index (PDI) of CUR-BBR/CSNH was remarkably low at 0.1883, in contrast to the higher PDI of 0.6 observed for CSNH. A lower PDI indicates a more uniform particle size distribution in CUR-BBR/CSNH, suggesting enhanced stability of the formulation [57]. Moreover, uniform size distribution is critical for drug delivery systems as it minimizes aggregation and ensures consistent therapeutic outcomes. The zeta potential values for CUR-BBR/CSNH (35.1 mV) and CSNH (34.83 mV) were comparable, indicating that the inclusion of the CUR-BBR co-crystal did not significantly alter the surface charge of the nanohydrogel. The high positive zeta potential for both formulations suggests excellent colloidal stability due to strong electrostatic repulsion between particles, which helps prevent aggregation and prolongs the shelf life of the nanohydrogel system [58]. Moreover, a high zeta potential enhances interaction with negatively charged cell membranes, facilitating cellular uptake and improving therapeutic efficiency.

The entrapment efficiency of CUR-BBR/CSNH was exceptionally high at 99.68%, indicating the formulation's capability to encapsulate nearly the entire drug content effectively. This high efficiency minimizes drug wastage and ensures a controlled release profile, essential for sustained therapeutic effects. The superior encapsulation efficiency, combined with a stable size distribution and high zeta potential, underlines the robustness of the CUR-BBR/CSNH system as a promising drug delivery platform.

3.2.2 | X-Ray Diffraction (XRD)

The X-ray diffraction (XRD) patterns of CUR-BBR/CSNH and CSNH provide critical insights into the crystallinity and structural arrangement of the nanohydrogel system. CSNH exhibits a broad, diffuse pattern characteristic of an amorphous structure, consistent with the nature of chitosan-based hydrogels. In contrast, CUR-BBR/CSNH displays distinct minor crystalline peaks, reflecting the presence of CUR and BBR in co-crystalline domains within the chitosan-TPP matrix (Figure 7). These observations indicate that the intermolecular interactions between CUR, BBR, and the ionic crosslinks in the chitosan-TPP matrix lead to the stabilization of the nanocomposite system [36]. Overall, these results align with the high entrapment efficiency (99.68%), lower PDI (0.188), and higher zeta potential (35.1 mV) observed, supporting the hypothesis that this chitosan-based nanohydrogel system provides a suitable microenvironment for the encapsulation and stabilization of CUR-BBR co-crystals.

3.2.3 | Drug Release of CUR-BBR From CUR-BBR/CSNH

The drug release profiles of CUR-BBR and CUR-BBR/CSNH in phosphate-buffered saline (PBS) at pH 7.4 and pH 4.5 reveal a stark improvement in release efficiency when CUR-BBR is encapsulated within the chitosan-based nanohydrogel (CSNH). At physiological

pH (7.4), the CUR-BBR/CSNH formulation showed significantly higher cumulative release percentages compared to the CUR-BBR formulation across all time points (Figure 8A). After 48 h, CUR-BBR/CSNH achieved 93.69% release, compared to 70.55% for CUR-BBR, marking an approximate 23% improvement in drug release. The faster and more consistent release kinetics observed in CUR-BBR/CSNH can be attributed to the hydrophilic nature of chitosan and its ionic interactions with the encapsulated drug molecules, which may enhance drug solubility and facilitate release through the hydrogel matrix. The statistical analysis corroborates these findings, with all differences in release between the two formulations deemed highly significant ($p < 0.05$). At pH 4.5, which mimics the acidic tumor microenvironment, CUR-BBR/CSNH again exhibited superior release behavior compared to CUR-BBR (Figure 8B). After 48 h, the CUR-BBR/CSNH released 97.62% of the CUR-BBR, whereas only 73.63% of CUR-BBR was released for the control group. The enhanced release under acidic conditions is promising for cancer therapy, as the formulation aligns well with the acidic pH of tumor tissues. The nanohydrogel's ability to swell more in acidic environments likely contributed to this enhanced release profile. Notably, there were no significant differences in the release profiling between the two groups at 30 min ($p > 0.05$).

The improved release profile of CUR-BBR/CSNH over CUR-BBR in both pH conditions underscores the potential of CSNH as an effective delivery vehicle for hydrophobic drugs [59]. Enhanced release under physiological conditions suggests better systemic bioavailability, while the pH-responsive release under acidic conditions makes CUR-BBR/CSNH an excellent candidate for site-specific drug delivery in cancer therapy.

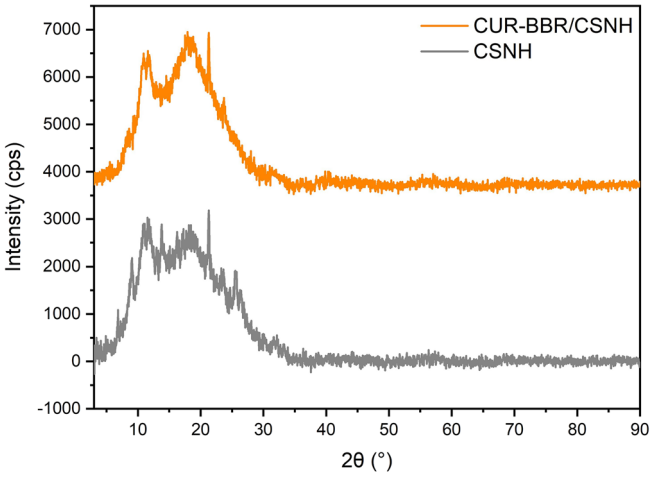

FIGURE 7 | X-ray diffraction patterns of CUR-BBR/CSNH (orange) and CSNH (grey) recorded over 3°–90°2θ.

3.3 | In Vitro Studies

3.3.1 | Cytotoxicity Assay (MTT)

The MTT cytotoxicity results highlight the varying anti-cancer potentials of different treatments against HEC-59 cancer cells (Table 3). Curcumin exhibits weak activity, with a high IC50 of 274.6 μg/mL, indicating poor efficacy as a standalone treatment. Berberine demonstrates improved cytotoxicity, with an IC50 of 62.9 μg/mL, reflecting moderate potency but still falling short compared to more advanced formulations.

TABLE 3 | Cytotoxic results for CUR, BBR, CUR/BBR co-crystals, and nanohydrogel formulation, compared against the reference drug, Camptothecin.

Treatment	IC_{50} (μg/mL)
	HEC-59
Curcumin	274.6 ± 2.4
Berberine	62.9 ± 1.7
Co-crystals	20.3 ± 1.3
Nanohydrogel-co-crystals	12.36 ± 0.44
Blank nanohydrogel	> 400
Camptothecin (Std.)	17.27 ± 2.7

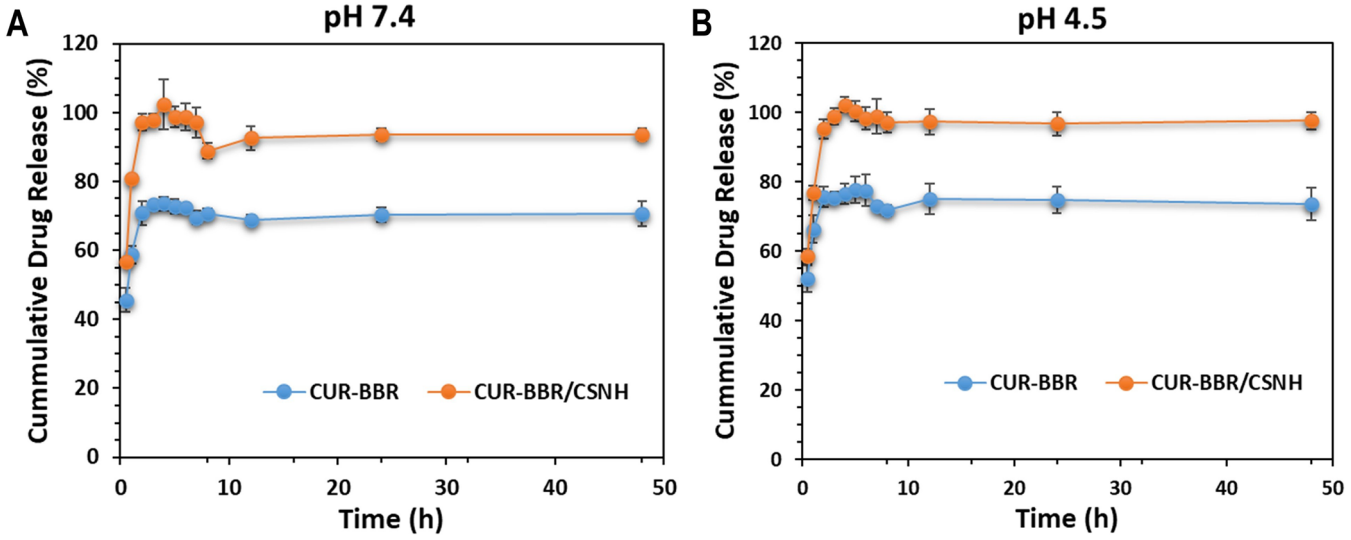

FIGURE 8 | Graph of mean drug release profiles with standard deviation of CUR-BBR from CUR-BBR/CSNH in PBS at pH (A) 7.4 and (B) 4.5.

The introduction of co-crystals significantly enhances the anti-cancer activity, reducing the IC50 to 20.3 μg/mL, likely due to improved solubility, bioavailability, and stability of the active compounds. The dual combination of curcumin (CUR) and berberine (BRR) demonstrates a synergistic effect, which may arise pharmacokinetically through enhanced solubility, stability, and bioavailability, or pharmacodynamically via a dual binding mechanism involving interactions at both the active site and an allosteric site of caspase, as revealed by molecular modeling studies discussed in the following sections. The nanohydrogel formulation further amplifies this effect, achieving an IC50 of 12.36 μg/mL, which is lower than both the co-crystals and the standard drug, Camptothecin (IC50: 17.27 μg/mL). This superior performance can be attributed to the nanohydrogel delivery system, which enhances the targeted delivery and controlled release of the active compounds, optimizing their therapeutic effects. The blank nanohydrogel, with an IC50 > 400 μg/mL, confirms that the nanohydrogel matrix itself has minimal cytotoxicity, underscoring that the observed activity in the nanohydrogel-co-crystals formulation is due to the active ingredients rather than the carrier. Overall, the results demonstrate the remarkable potential of the nanohydrogel-co-crystals formulation as a highly effective anti-cancer treatment, surpassing the standard drug in potency while showcasing the value of advanced drug delivery systems in enhancing therapeutic outcomes.

3.3.2 | Caspase 3/7 Activity

The Caspase-Glo 3/7 assay results presented in Figure 9 provide valuable insights into the apoptotic potential of CUR/BBR, specifically co-crystals, nanohydrogel formulation, and the reference drug Camptothecin. The luminescence values in the assay are directly proportional to caspase 3/7 activity, a key indicator of apoptosis, making this data crucial for evaluating the pro-apoptotic efficacy of the formulation against endometrial cancer cells.

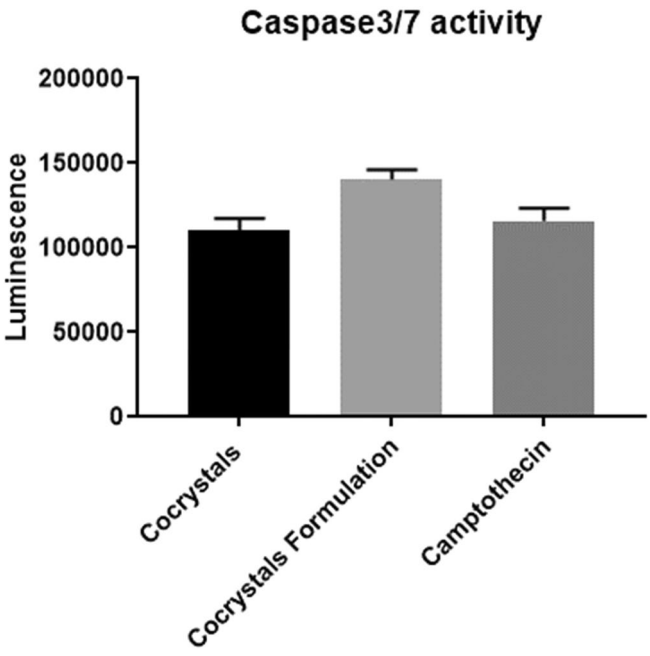

FIGURE 9 | Caspase 3/7 activity of CUR/BBR co-crystals and nanohydrogel formulation compared to the standard drug camptothecin.

The co-crystals exhibit luminescence levels of approximately 100,000, which are close to the values observed for the reference drug Camptothecin, demonstrating notable activation of caspase 3/7. In contrast, the nanohydrogel formulation displays significantly higher luminescence, exceeding 150,000, thereby surpassing both the raw co-crystals and Camptothecin. This remarkable increase in luminescence indicates that the formulation substantially enhances apoptotic activity, likely due to improved solubility, stability, and cellular uptake of the active compounds. The nanotechnology-based delivery system optimizes the release and bioavailability of the co-crystals, facilitating more efficient interaction with apoptotic pathways and resulting in higher caspase 3/7 activation.

3.4 | Molecular Modelling Studies

3.4.1 | CUR/BBR Co-Crystal Modelling

The optimized three-dimensional structure of the CUR/BBR complex shows the molecular structures of CUR and BBR (Figure S6A,B). Here, we can observe the specific functional groups involved in the interaction. For CUR, the presence of multiple hydroxyl groups (red atoms) suggests potential hydrogen bonding with BBR, which also contains nitrogen atoms (blue) and oxygen atoms (red) capable of forming such bonds. The proximity of these groups in the model implies a favorable interaction, likely contributing to the stability of the complex. Additionally, the aromatic rings in both molecules could engage in π-π interactions, stabilizing the configuration further. This detailed view highlights the molecular compatibility and potential synergistic effects due to the structural complementarity between CUR and BBR, which could lead to enhanced bioavailability and therapeutic efficacy when used in combination.

3.4.2 | Molecular Docking Analysis of CUR and BBR to Caspase-3

The docking results reveal distinct binding affinities of curcumin (CUR) and berberine (BBR) to caspase-3, highlighting their potential roles in both covalent and non-covalent interactions (Table 4). Non-covalent docking using AutoDock Vina shows strong binding at the active site for CUR_{act} (−7.1 kcal/mol) and BBR_{act} (−7.3 kcal/mol), indicating their comparable affinity to caspase-3. Blind docking results are consistent, with CUR_{act} and BBR_{act} achieving comparable scores (−7.0 and −7.3 kcal/mol, respectively), suggesting stable interactions irrespective of predefined docking regions. Covalent docking results from Glide indicate CURact forms a stronger covalent interaction with Cys163 (−3.06 kcal/mol) compared to CUR_{alst} binding at Cys264 (−0.33 kcal/mol). These findings underscore the preference of CUR_{act} for the active site, aligning with its higher non-covalent binding affinity. Notably, BBR_{alst} exhibits moderate non-covalent binding (−6.3 kcal/mol), complementing CUR_{act} covalent interactions. Overall, the docking data underscore the potential of curcumin and berberine as complementary inhibitors of caspase-3.

Furthermore, the binding interactions of curcumin (CUR), berberine (BBR), and their co-binding to caspase-3 were analyzed to elucidate their inhibitory mechanisms (Figure 10). CUR bonded

covalently at the active site of caspase-3 by forming a stable interaction with the catalytic residue CYS163, rendering irreversible inhibition. This covalent interaction interrupts substrate accessibility and enzymatic activity. Additionally, conventional hydrogen bonds with GLY122 and GLN161, along with a pi-sulfur interaction with MET61 and van der Waals contacts, further anchor CUR within the active site pocket. On the other hand, berberine bonded non-covalently at the allosteric site and stabilized itself through key hydrogen bonds with GLU124 and LYS137, pi-stacking interactions with TYR195 and TYR197, and van der Waals contacts involving THR140, GLY125, MET268, and VAL266. The allosteric binding of berberine may likely induce conformational changes in caspase-3, impairing its catalytic function by preventing the enzyme from adopting a fully active conformation. In the co-binding mode, CUR and BBR simultaneously occupy their respective binding sites without steric clashes, offering a dual-site inhibitory mechanism. This dual-site engagement results in a synergistic inhibitory effect, as the active site is blocked irreversibly, and the allosteric modulation further suppresses enzymatic activity. We can hypothesize that the dual-site inhibitory strategy may enhance the overall potency of caspase-3 suppression and minimize the risk of resistance often associated with single-site targets. These findings provide a strong rationale for the design of dual covalent/non-covalent inhibitors as an effective strategy to induce apoptosis in endometrial cancer cells.

TABLE 4 | Docking scores (kcal/mol) of CUR and BBR at both the catalytic and allosteric sites of caspase-3, computed with Autodock Vina and Glide.

Non-covalent docking (autodock vina)		
Caspase-3 complex	**X-ray-site-directed docking**	**Blind docking**
CUR_{act}	−7.1	−7.0
BBR_{act}	−7.3	−7.3
CUR_{alst}	−5.3	
BBR_{alst}	−6.3	
Covalent docking (Glide)		
CUR_{act}	−3.06	C163 (Nucleophilic residue)
CUR_{alst}	−0.33	C264 (Nucleophilic residue)

3.4.3 | Molecular Dynamics and Thermodynamic Binding Affinity Analysis

3.4.3.1 | Conformational Dynamics of Casapse-3. The structural stability and flexibility of the systems were analyzed through RMSD and RMSF, revealing critical insights into the dynamics of the unbound caspase-3 (apo), BBR, CUR, and CUR-BBR systems during the 200 ns MD simulation (Figure 11). The RMSD values highlight the stability of the protein-ligand complexes, with the apo system exhibiting a moderate RMSD of 1.653 Å. The BBR system demonstrates

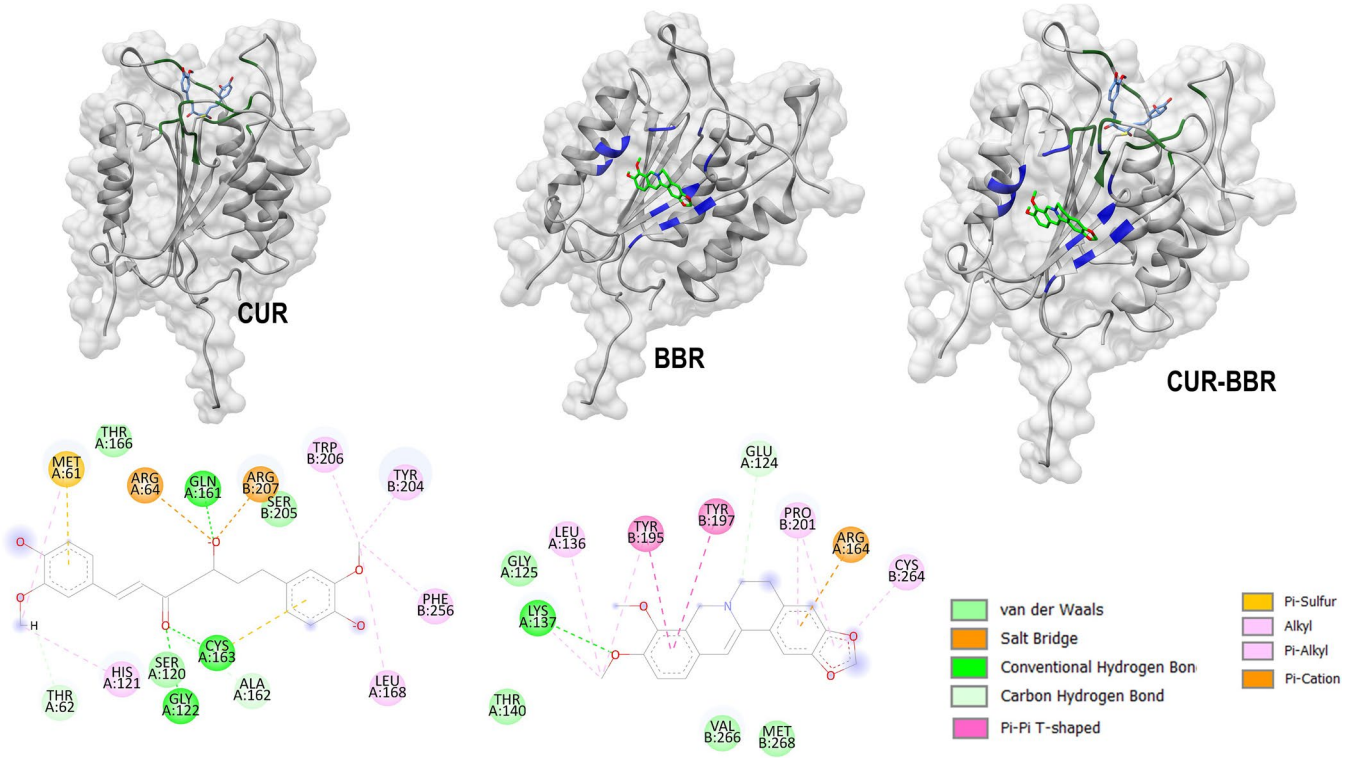

FIGURE 10 | *Top panel*: The 3D docking poses of CUR (sky blue) and BBR (spring green) interacting with the catalytic residues (dark green) and allosteric residues (blue) of caspase-3 (grey). *Bottom panel*: The 2D protein-ligand interaction profiles of CUR and BBR at the active site and allosteric site, respectively, showing the different types of interaction forces.

slightly higher stability with an RMSD of 1.512 Å, suggesting that the binding of BBR contributes to minimal structural perturbation. In contrast, the CUR system shows a higher RMSD of 2.037 Å, indicating greater conformational deviations, likely due to increased dynamics. Notably, the CUR-BBR system stabilizes caspase-3 with a mean RMSD of 1.656 Å, comparable to the apo system (Figure 11B). This stabilization suggests a synergistic effect between CUR and BBR, mitigating the pronounced conformational changes observed with CUR alone. The RMSF analysis further supports these findings by highlighting the degrees of flexibility of the individual residues. The apo system exhibits moderate flexibility with an RMSF of 0.858 Å, while the BBR system slightly reduces flexibility to 0.842 Å, indicative of stabilizing interactions. Similarly, CUR shows an RMSF of 0.850 Å, which is comparable to the apo system. Notably, the CUR-BBR system exhibits the least flexibility, with an RMSF of 0.743 Å, demonstrating a remarkable ability to stabilize the protein and restrict motion (Figure 11A).

Taken together, these results underscore the potential of the CUR-BBR co-crystal to enhance protein stability and minimize fluctuations compared to CUR or BBR alone. The reduced RMSD and RMSF values for the CUR-BBR system indicate improved binding and prolonged interaction time, which are crucial for effective therapeutic outcomes.

3.4.3.2 | Binding Free Energy Calculations. The binding free energy (ΔG_{bind}) calculations of CUR and BBR highlight the inhibitory synergistic effects against caspase-3 (Table 5). The CUR_{act} and BBR_{alst} systems were evaluated using MM/GBSA, and the results illustrate distinct contributions from van der Waals (ΔE_{vdW}), electrostatic (ΔE_{elec}), polar solvation (ΔG_{GB}), and non-polar solvation (ΔG_{SA}) energies. Additionally, the combined system was also analyzed to simulate their co-binding effects, mimicking the in vitro impact of the co-crystals.

The combined system of CUR_{act}-BBR_{alst} revealed enhanced binding affinity profiles when compared to individual binding profiles. The ΔG_{bind} of CUR_{act} in the individual binding system was −29.16 kcal/mol, while BBR_{alst} showed a ΔG_{bind} of −11.93 kcal/mol. In co-binding, CUR_{act} demonstrated a ΔG_{bind} of −31.78 kcal/mol, while BBR_{alst} exhibited a ΔG_{bind} of −15.90 kcal/mol. This observation may be due to the fact that CUR primarily anchors the binding complex, while BBR provides

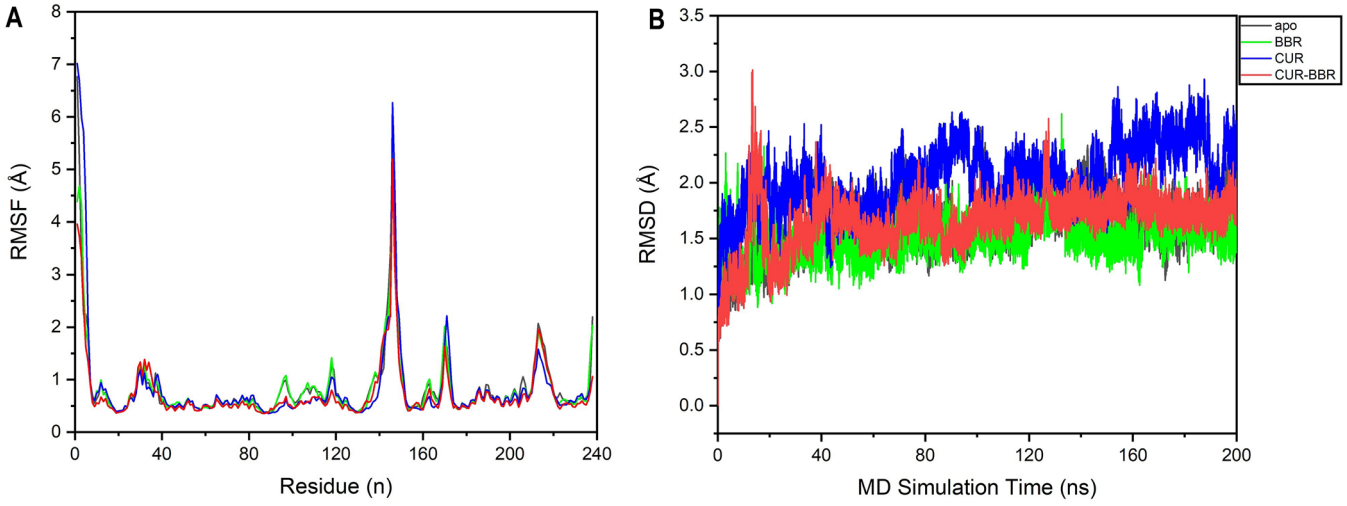

FIGURE 11 | Graph of (A) RMSF and (B) RMSD of unbound caspase-3 (apo) (black) compared to when bound to BBR at the allosteric site (green), CUR at the active site (blue), and CUR and BBR in a co-binding configuration (red). Computations were made across 200 ns MD simulations.

TABLE 5 | Binding free energy terms of CUR_{act} and BBR_{alst} complexes expressed in kcal/mol with the standard error of the mean. MM/GBSA was employed using 50,000 MD trajectory frames.

Complex system	Energy components (kcal/mol)[a]						
	ΔE_{vdW}	ΔE_{elec}	ΔG_{GB}	ΔG_{SA}	ΔG_{gas}	ΔG_{solv}	ΔG_{bind}
Co-binding CUR_{act}-BBR_{alst}							
CUR_{act}	−33.14 ± 0.08	−32.89 ± 0.11	39.07 ± 0.08	−4.82 ± 0.01	−66.03 ± 0.12	34.25 ± 0.07	−31.78 ± 0.09
BBR_{alst}	−23.20 ± 0.12	27.50 ± 0.31	−16.89 ± 0.33	−3.30 ± 0.02	4.30 ± 0.37	−20.20 ± 0.32	−15.90 ± 0.09
Individual CUR_{act} & BBR_{last}							
CUR_{act}	−35.98 ± 0.09	−22.17 ± 0.20	33.84 ± 0.14	−4.85 ± 0.01	−58.15 ± 0.22	28.99 ± 0.14	−29.16 ± 0.13
BBR_{alst}	−18.92 ± 0.10	6.87 ± 0.34	2.44 ± 0.33	−2.33 ± 0.02	−12.05 ± 0.31	0.12 ± 0.34	−11.93 ± 0.10

[a]ΔE_{elec} (electrostatic energy), ΔE_{vdW} (van der Waals energy), ΔG_{GB} (polar solvation energy), ΔG_{SA} (non-polar solvation energy), ΔG_{gas} (gas-phase energy), ΔG_{solv} (Total solvation free energy of polar and non-polar states), and ΔG_{bind} (total free binding energy).

complementary interactions that may stabilize the system in a dynamic equilibrium, likely due to optimized spatial arrangements in the co-binding scenario.

The co-binding analysis aligns with the hypothesis that CUR and BBR can synergistically enhance caspase-3 targeting, reflecting the observed in vitro efficacy of the CUR-BBR co-crystals in inducing apoptosis. The dual engagement of active and allosteric sites by CUR and BBR likely amplifies the apoptotic signaling cascade, overcoming the limitations of individual components. The combined interaction at caspase-3 may also reduce the risk of resistance development, offering a robust therapeutic strategy for endometrial cancer treatment.

4 | Conclusion

The study highlights the innovative design and therapeutic potential of curcumin (CUR) and berberine (BBR) co-crystals encapsulated in a nanohydrogel for endometrial cancer treatment. This dual pharmacokinetic and pharmacodynamic strategy enhances drug solubility, stability, and bioavailability, while leveraging complementary mechanisms of action. CUR binds covalently to the active site of caspase-3, while BBR interacts non-covalently at an allosteric site, achieving synergistic inhibition of caspase-3 and triggering enhanced apoptosis.

The nanohydrogel formulation significantly improves the cytotoxic activity of CUR-BBR co-crystals, achieving an IC50 of 12.36 μg/mL against HEC-59 cells, outperforming the co-crystals alone and the reference drug Camptothecin. Caspase-Glo 3/7 assays confirm higher luminescence for the nanohydrogel, indicating superior apoptotic activity. Molecular docking and dynamics simulations validate the dual binding mechanism, demonstrating high binding affinity and stability of CUR-BBR interactions with caspase-3. This dual-binding approach also minimizes protein flexibility, enhancing the inhibitory effect and reducing the risk of resistance.

In conclusion, the CUR-BBR nanohydrogel represents a robust and innovative therapeutic strategy, integrating advanced drug delivery with a dual-targeting mechanism to maximize anticancer efficacy. This study provides a foundation for future clinical development of multi-targeted cancer therapies.

Author Contributions

All authors have contributed equally to the study design, experimental work, data analysis, manuscript writing, and revision. All authors approved and agreed on publication.

Ethics Statement

The authors have nothing to report.

Consent

The authors have nothing to report.

Conflicts of Interest

The authors declare no conflicts of interest.

Data Availability Statement

The data that support the findings of this study are available from the corresponding author upon reasonable request.

References

1. V. Makker, H. MacKay, I. Ray-Coquard, et al., "Endometrial Cancer," *Nature Reviews Disease Primers. Nature Research* 7 (2021): 88, https://doi.org/10.1038/s41572-021-00324-8.

2. H. Baker-Rand and S. J. Kitson, "Recent Advances in Endometrial Cancer Prevention, Early Diagnosis and Treatment," *Cancers* 16, no. 5 (2024): 1028, https://doi.org/10.3390/cancers16051028.

3. P. Soberanis Pina and S. Lheureux, "Novel Molecular Targets in Endometrial Cancer: Mechanisms and Perspectives for Therapy," in *Biologics: Targets and Therapy*, vol. 18 (Dove Medical Press Ltd, 2024), 79–93, https://doi.org/10.2147/BTT.S369783.

4. G. Giannone, L. Attademo, G. Scotto, et al., "Endometrial Cancer Stem Cells: Role, Characterization and Therapeutic Implications," *Cancers* 11, no. 11 (2019): 1820, https://doi.org/10.3390/cancers11111820.

5. C. Kyathanahalli, K. Organ, R. S. Moreci, et al., "Uterine Endoplasmic Reticulum Stress-Unfolded Protein Response Regulation of Gestational Length Is Caspase-3 and-7-Dependent," *Proceedings of the National Academy of Sciences of the United States of America* 112, no. 45 (2015): 14090–14095, https://doi.org/10.1073/PNAS.1518309112.

6. S. E. Garvin, C. Kyathanahalli, S. Soha, J. C. Condon, and P. Jeyasuria, "Preimplantation Apoptotic Endometrial Caspase-3–Mediated Phospholipase A2 Activation: A Potential Component in Programming Uterine Receptivity," *F&S Science* 4, no. 2 (2023): 141–150, https://doi.org/10.1016/J.XFSS.2022.12.003.

7. J. E. Vince, D. De Nardo, W. Gao, et al., "The Mitochondrial Apoptotic Effectors BAX/BAK Activate Caspase-3 and -7 to Trigger NLRP3 Inflammasome and Caspase-8 Driven IL-1β Activation," *Cell Reports* 25, no. 9 (2018): 2339–2353, https://doi.org/10.1016/J.CELREP.2018.10.103.

8. X. Liu, Y. He, F. Li, et al., "Caspase-3 Promotes Genetic Instability and Carcinogenesis," *Molecular Cell* 58, no. 2 (2015): 284–296, https://doi.org/10.1016/J.MOLCEL.2015.03.003.

9. R. Zhuang and H. Liu, "Mechanism of Regulation of KIF23 on Endometrial Cancer Cell Growth and Apoptosis," *Discover Oncology* 15, no. 1 (2024): 1–13, https://doi.org/10.1007/S12672-024-00937-X.

10. H. G. Häcker, M. T. Sisay, and M. Gütschow, "Allosteric Modulation of Caspases," *Pharmacology and Therapeutics* 132 (2011): 180–195, https://doi.org/10.1016/j.pharmthera.2011.07.003.

11. J. A. Hardy, J. Lam, J. T. Nguyen, T. O'Brien, and J. A. Wells, "Discovery of an Allosteric Site in the Caspases," *Proceedings of the National Academy of Sciences of the United States of America* 101, no. 34 (2004): 12461–12466, https://doi.org/10.1073/pnas.0404781101.

12. A. Doostmohammadi, H. Jooya, K. Ghorbanian, S. Gohari, and M. Dadashpour, "Potentials and Future Perspectives of Multi-Target Drugs in Cancer Treatment: The Next Generation Anti-Cancer Agents," *Cell Communication and Signaling* 22, no. 1 (2024): 1–22, https://doi.org/10.1186/S12964-024-01607-9.

13. N. M. Raghavendra, D. Pingili, S. Kadasi, A. Mettu, and S. V. U. M. Prasad, "Dual or Multi-Targeting Inhibitors: The Next Generation Anticancer Agents," *European Journal of Medicinal Chemistry* 143 (2018): 1277–1300, https://doi.org/10.1016/J.EJMECH.2017.10.021.

14. J. Mandal, T. N. Jones, J. M. Liberto, S. Gaillard, T.-L. Wang, and I.-M. Shih, "Dual Inhibition of SYK and EGFR Overcomes Chemoresistance by Inhibiting CDC6 and Blocking DNA Replication," *Cancer Research* 84, no. 22 (2024): 3881–3893, https://doi.org/10.1158/0008-5472.CAN-24-0769/746930/AM/DUAL-INHIBITION-OF-SYK-AND-EGFR-OVERCOMES.

15. C. Kim, H. Ludewig, A. Hadzipasic, S. Kutter, V. Nguyen, and D. Kern, "A Biophysical Framework for Double-Drugging Kinases,"

Proceedings of the National Academy of Sciences of the United States of America 120, no. 34 (2023): e2304611120, https://doi.org/10.1073/PNAS.2304611120.

16. H. Zhang, M. Zhu, M. Li, et al., "Mechanistic Insights Into Co-Administration of Allosteric and Orthosteric Drugs to Overcome Drug-Resistance in T315I BCR-ABL1," *Frontiers in Pharmacology* 13 (2022): 862504, https://doi.org/10.3389/FPHAR.2022.862504.

17. G. Elamin, A. Aljoundi, and M. E. S. Soliman, "Co-Binding of JQ1 and Venetoclax Exhibited Synergetic Inhibitory Effect for Cancer Therapy; Potential Line of Treatment for the Waldenström Macroglobulinemia Lymphoma," *Chemistry & Biodiversity* 19, no. 7 (2022): e202100845, https://doi.org/10.1002/CBDV.202100845.

18. E. Oduro-Kwateng, A. H. Rabbad, and M. E. Soliman, "The Juxtaposition of Allosteric and Catalytic Inhibition in PLK1: Tradeoff for Chemotherapy and Thermodynamic Profiles of KBJK557 and BI 6727," *Journal of Computational Biophysics and Chemistry* 23, no. 3 (2024): 379–401, https://doi.org/10.1142/S2737416523500680.

19. Y. Song, Q. Cai, M. Jiang, et al., "A Novel Dual Covalent and Non-Covalent Next Generation Inhibitor of Bruton's Tyrosine Kinase LP-168 in Patients With Relapsed/Refractory B Cell Non-Hodgkin Lymphoma: Safety and Efficacy Results From a Phase 1 Study," *Blood* 142, no. Supplement 1 (2023): 4400, https://doi.org/10.1182/BLOOD-2023-180485.

20. B. Gordon, E. Muhowski, J. Ravikrishnan, et al., "Targeting Covalent and Non-Covalent Btki-Resistant CLL Using the Dual Irreversible/Reversible 4th Generation BTK Inhibitor LP-168," *Blood* 142 (2023): 416, https://doi.org/10.1182/BLOOD-2023-178259.

21. S. Hu, M. Ferraro, A. P. Thomas, et al., "Dual Binding to Orthosteric and Allosteric Sites Enhances the Anticancer Activity of a TRAP1-Targeting Drug," *Journal of Medicinal Chemistry* 63, no. 6 (2020): 2930–2940, https://doi.org/10.1021/ACS.JMEDCHEM.9B01420/SUPPL_FILE/JM9B01420_SI_005.CSV.

22. R. O. Kumi, C. Agoni, M. A. A. Ibrahim, and M. E. S. Soliman, "Dual Enzymatic Inhibitory Mechanism of WM382 on Plasmepsin IX and X: Atomistic Perspectives From Dynamic Analysis," *Informatics in Medicine Unlocked* 29 (2022): 100874, https://doi.org/10.1016/J.IMU.2022.100874.

23. V. Zoi, V. Galani, G. D. Lianos, S. Voulgaris, A. P. Kyritsis, and G. A. Alexiou, "The Role of Curcumin in Cancer Treatment," *Biomedicine* 9, no. 9 (2021): 1086, https://doi.org/10.3390/BIOMEDICINES9091086.

24. S. A. Almatroodi, M. A. Alsahli, and A. H. Rahmani, "Berberine: An Important Emphasis on Its Anticancer Effects Through Modulation of Various Cell Signaling Pathways," *Molecules* 27, no. 18 (2022): 5889, https://doi.org/10.3390/MOLECULES27185889.

25. K. Wang, C. Zhang, J. Bao, et al., "Synergistic Chemopreventive Effects of Curcumin and Berberine on Human Breast Cancer Cells Through Induction of Apoptosis and Autophagic Cell Death," *Scientific Reports* 6, no. 1 (2016): 1–14, https://doi.org/10.1038/srep26064.

26. P. Maiti, A. Plemmons, and G. L. Dunbar, "Combination Treatment of Berberine and Solid Lipid Curcumin Particles Increased Cell Death and Inhibited PI3K/Akt/mTOR Pathway of Human Cultured Glioblastoma Cells More Effectively Than Did Individual Treatments," *PLoS One* 14, no. 12 (2019): e0225660, https://doi.org/10.1371/JOURNAL.PONE.0225660.

27. T. Murakami, E. Bodor, and N. Bodor, "Approaching Strategy to Increase the Oral Bioavailability of Berberine, a Quaternary Ammonium Isoquinoline Alkaloid: Part 1. Physicochemical and Pharmacokinetic Properties," *Expert Opinion on Drug Metabolism & Toxicology* 19, no. 3 (2023): 129–137, https://doi.org/10.1080/17425255.2023.2203857.

28. M. Hegde, S. Girisa, B. BharathwajChetty, R. Vishwa, and A. B. Kunnumakkara, "Curcumin Formulations for Better Bioavailability: What We Learned From Clinical Trials Thus Far?," *ACS Omega* 8 (2023): 10713–10746, https://doi.org/10.1021/acsomega.2c07326.

29. L. Devi, H. Chopra, and P. Gaba, "Nanohydrogels for Targeted Drug Delivery Systems," *Bionanotechnology: Emerging Applications of Bionanomaterials* 23 (2022): 333–356, https://doi.org/10.1016/B978-0-12-823915-5.00003-4.

30. A. C. Yu, H. Chen, D. Chan, et al., "Scalable Manufacturing of Biomimetic Moldable Hydrogels for Industrial Applications," *Proceedings of the National Academy of Sciences of the United States of America* 113, no. 50 (2016): 14255–14260, https://doi.org/10.1073/PNAS.1618156113.

31. M. Kaur, A. Bains, P. Chawla, et al., "Milk Protein-Based Nanohydrogels: Current Status and Applications," *Gels* 8, no. 7 (2022): 432, https://doi.org/10.3390/GELS8070432.

32. S. Jung, I. Choi, and I. W. Kim, "Liquid-Assisted Grinding to Prepare a Cocrystal of Adefovir Dipivoxil Thermodynamically Less Stable Than Its Neat Phase," *Crystals* 5, no. 4 (2015): 583–591, https://doi.org/10.3390/cryst5040583.

33. S. J. Bethune, N. Schultheiss, and J. O. Henck, "Improving the Poor Aqueous Solubility of Nutraceutical Compound Pterostilbene Through Cocrystal Formation," *Crystal Growth and Design* 11, no. 7 (2011): 2817–2823, https://doi.org/10.1021/cg1016092.

34. H. Wang, C. Zheng, F. Tian, et al., "Improving the Dissolution Rate and Bioavailability of Curcumin via Co-Crystallization," *Pharmaceuticals* 17, no. 4 (2024): 489, https://doi.org/10.3390/ph17040489.

35. M. S. T. Abdul Azeeze, S. Kandasamy, P. Palanisamy, P. Palanichamy, and M. Subramania Nainar, "Cocrystallization of Dasatinib With Different Acids Improves the Solubility and Physicochemical Properties: A Combined Experimental and Theoretical Studies," *Chemical Physics Impact* 7 (2023): 100247, https://doi.org/10.1016/j.chphi.2023.100247.

36. S. Abbaszadeh, M. Rashidipour, P. Khosravi, et al., "Biocompatibility, Cytotoxicity, Antimicrobial and Epigenetic Effects of Novel Chitosan-Based Quercetin Nanohydrogel in Human Cancer Cells," *International Journal of Nanomedicine* 15 (2020): 5963–5975, https://doi.org/10.2147/IJN.S263013.

37. B. Farasati Far, M. Omrani, M. R. Naimi Jamal, and S. Javanshir, "Multi-Responsive Chitosan-Based Hydrogels for Controlled Release of Vincristine," *Communications Chemistry* 6, no. 1 (2023): 28, https://doi.org/10.1038/s42004-023-00829-1.

38. Y. S. Loo, T. Madheswaran, R. Rajendran, and R. J. Bose, "Encapsulation of Berberine Into Liquid Crystalline Nanoparticles to Enhance Its Solubility and Anticancer Activity in MCF7 Human Breast Cancer Cells," *Journal of Drug Delivery Science and Technology* 57 (2020): 101756, https://doi.org/10.1016/j.jddst.2020.101756.

39. E. Babaeenezhad, M. Rashidipour, Z. Jangravi, M. Moradi Sarabi, and A. Shahriary, "Cytotoxic and Epigenetic Effects of Berberine-Loaded Chitosan/Pectin Nanoparticles on AGS Gastric Cancer Cells: Role of the miR-185-5p/KLF7 Axis, DNMTs, and Global DNA Methylation," *International Journal of Biological Macromolecules* 260 (2024): 129618, https://doi.org/10.1016/j.ijbiomac.2024.129618.

40. K. Kasumbwe, N. Venugopala, V. Mohanlall, and B. Odhav, "Synthetic Mono/di-Halogenated Coumarin Derivatives and Their Anticancer Properties," *Anti-Cancer Agents in Medicinal Chemistry* 17, no. 2 (2016): 276–285, https://doi.org/10.2174/1871520616666160926112508.

41. P. Olszewska, D. Cal, P. Zagórski, and E. Mikiciuk-Olasik, "A Novel Trifluoromethyl 2-Phosphonopyrrole Analogue Inhibits Human Cancer Cell Migration and Growth by Cell Cycle Arrest at G1 Phase and Apoptosis," *European Journal of Pharmacology* 871 (2020): 172943, https://doi.org/10.1016/j.ejphar.2020.172943.

42. B. Kaya, L. Yurttaş, M. Baysal, B. Korkut Çelikateş, Z. A. Kaplancıklı, and R. İmamoğlu, "Synthesis and Anticancer Activity Evaluation of Some Novel Imidazo[1,2-a]Pyridine Based Heterocycles Containing S-Alkyl/Aryl Moiety," *Phosphorus, Sulfur and Silicon and the Related Elements* 199, no. 5 (2024): 383–393, https://doi.org/10.1080/10426507.2024.2349305.

43. H. Nakatsumi and S. Yonehara, "Identification of Functional Regions Defining Different Activity in Caspase-3 and Caspase-7 Within

Cells," *Journal of Biological Chemistry* 285, no. 33 (2010): 25418–25425, https://doi.org/10.1074/jbc.M110.126573.

44. E. F. Pettersen, T. D. Goddard, C. C. Huang, et al., "UCSF Chimera - A Visualization System for Exploratory Research and Analysis," *Journal of Computational Chemistry* 25, no. 13 (2004): 1605–1612, https://doi.org/10.1002/jcc.20084.

45. J. C. Gordon, J. B. Myers, T. Folta, V. Shoja, L. S. Heath, and A. Onufriev, "H++: A Server for Estimating pKas and Adding Missing Hydrogens to Macromolecules," *Nucleic Acids Research* 33, no. Web Server (2005): W368–W371, https://doi.org/10.1093/nar/gki464.

46. M. V. Shapovalov and R. L. Dunbrack, "A Smoothed Backbone-Dependent Rotamer Library for Proteins Derived From Adaptive Kernel Density Estimates and Regressions," *Structure* 19, no. 6 (2011): 844–858, https://doi.org/10.1016/j.str.2011.03.019.

47. S. S. Butt, Y. Badshah, M. Shabbir, and M. Rafiq, "Molecular Docking Using Chimera and Autodock Vina Software for Nonbioinformaticians," *JMIR Bioinformatics and Biotechnology* 1, no. 1 (2020): e14232, https://doi.org/10.2196/14232.

48. K. Zhu, K. W. Borrelli, J. R. Greenwood, et al., "Docking Covalent Inhibitors: A Parameter Free Approach to Pose Prediction and Scoring," *Journal of Chemical Information and Modeling* 54, no. 7 (2014): 1932–1940, https://doi.org/10.1021/ci500118s.

49. R. Salmon-Ferrer, A. W. Goetz, D. Poole, S. Le Grand, and R. C. Walker, "Routine Microsecond Molecular Dynamics Simulations With AMBER - Part II: Particle Mesh Ewald," *Journal of Chemical Theory and Computation* 9, no. 9 (2013): 3878–3888.

50. D. R. Roe and T. E. Cheatham, "PTRAJ and CPPTRAJ: Software for Processing and Analysis of Molecular Dynamics Trajectory Data," *Journal of Chemical Theory and Computation* 9, no. 7 (2013): 3084–3095, https://doi.org/10.1021/ct400341p.

51. E. Wang, H. Sun, J. Wang, et al., "End-Point Binding Free Energy Calculation With MM/PBSA and MM/GBSA: Strategies and Applications in Drug Design," *Chemical Reviews* 119 (2019): 9478–9508, https://doi.org/10.1021/acs.chemrev.9b00055.

52. J. Pantwalawalkar, H. More, D. Bhange, U. Patil, and N. Jadhav, "Novel Curcumin Ascorbic Acid Cocrystal for Improved Solubility," *Journal of Drug Delivery Science and Technology* 61 (2021): 102233, https://doi.org/10.1016/j.jddst.2020.102233.

53. Q. Lu, J. Dun, J. M. Chen, S. Liu, and C. C. Sun, "Improving Solid-State Properties of Berberine Chloride Through Forming a Salt Cocrystal With Citric Acid," *International Journal of Pharmaceutics* 554 (2019): 14–20, https://doi.org/10.1016/j.ijpharm.2018.10.062.

54. E. H. Ismail, D. Y. Sabry, H. Mahdy, and M. M. H. Khalil, "Synthesis and Characterization of Some Ternary Metal Complexes of Curcumin With 1,10-Phenanthroline and Their Anticancer Applications," *Journal of Scientific Research* 6, no. 3 (2014): 509–519, https://doi.org/10.3329/jsr.v6i3.18750.

55. S. K. Battu, M. A. Repka, S. Maddineni, A. G. Chittiboyina, M. A. Avery, and S. Majumdar, "Physicochemical Characterization of Berberine Chloride: A Perspective in the Development of a Solution Dosage Form for Oral Delivery," *AAPS PharmSciTech* 11, no. 3 (2010): 1466–1475, https://doi.org/10.1208/s12249-010-9520-y.

56. A. Narmani and S. M. Jafari, "Chitosan-Based Nanodelivery Systems for Cancer Therapy: Recent Advances," *Carbohydrate Polymers* 272 (2021): 118464, https://doi.org/10.1016/j.carbpol.2021.118464.

57. M. Danaei, M. Dehghankhold, S. Ataei, et al., "Impact of Particle Size and Polydispersity Index on the Clinical Applications of Lipidic Nanocarrier Systems," *Pharmaceutics* 10, no. 2 (2018): 57, https://doi.org/10.3390/pharmaceutics10020057.

58. S. Honary and F. Zahir, "Effect of Zeta Potential on the Properties of Nano-Drug Delivery Systems - A Review (Part 2)," *Tropical Journal of Pharmaceutical Research* 12, no. 2 (2013): 265–273, https://doi.org/10.4314/tjpr.v12i2.20.

59. N. M. Alsawaftah, N. S. Awad, W. G. Pitt, and G. A. Husseini, "pH-Responsive Nanocarriers in Cancer Therapy," *Polymers* 14 (2022): 936, https://doi.org/10.3390/polym14050936.

Supporting Information

Additional supporting information can be found online in the Supporting Information section.